Studies on the application of *Bombyx mori* cypovirus polyhedra

Junji Shimabukuro

Contents

Chapter 1: General Introduction

Cytoplasmic polyhedrosis viruses (CPVs) belong to the genus Cypovirus of the family *Reoviridae* (Mertens et al., 2004a, b) Viruses belonging to the family *Reoviridae* are characterized by the presence of capsids made up of concentric icosahedrally symmetric layers of proteins organized in one, two or three shells containing 10 to 12 segments of linear, double-stranded RNA (dsRNA). Members of the *Reoviridae* are grouped into 12 distinct genera, Orthoreovirus, Orbivirus, Rotavirus, Coltivirus, Aquareovirus, Cypovirus, Fijivirus, Mycoreovirus, Phytoreovirus, Oryzavirus, Seadornavirus and Idnoreovirus (Belloncik, 1989; Belloncik and Mori, 1998; Payne and Mertens, 1983). The natural hosts of the *Reoviridae* include vertebrates, invertebrates, and plants. The virulence they exhibit toward these hosts differs widely. Insect larvae infected by CPV are characterized by the production of massive amounts of polyhedrin protein, which crystallizes in the cell cytoplasm forming occlusion bodies named polyhedra that each incorporates numerous virus particles (Fig. 1A). CPVs are unique amongst the *Reoviridae* because of this unusual encapsulation of virus within protein micro-crystals and also because the virus particles have only a single capsid shell.

CPVs have been isolated from more than 250 species of insects (Hukuhara and Bohami, 1991). Different cypovirus "types" were initially identified on the basis of differences in the migration patterns of the genome segments during polyacrylamide gel electrophoresis, i.e., electropherotypes (Belloncik, 1989; Belloncik and Mori, 1998; Li et al., 2006; Li et al., 2007; Payne and Mertens, 1983; Shapiro et al., 2005; Tan et al., 2008). Subsequent studies showed a good correlation between electropherotype and the grouping of strains on the basis of serological properties or RNA cross-hybridization. More recently, nucleotide sequences, for example, those of the genome segment encoding polyhedrin, are used to distinguish different *Cypovirus* types. Twenty *Cypovirus* types are currently recognized (Graham et al., 2006; Mertens et al., 2004a, b). The complete nucleotide sequence of *Bombyx mori* CPV (BmCPV)

from type 1 was the first to be determined (Arella et al., 1988; Hagiwara et al., 2001; Hagiwara and Matsumoto, 2000; Hagiwara et al., 2002; Hagiwara et al., 1998a; Hagiwara et al., 1998b; Ikeda et al., 2001; Mori et al., 1989; Mori et al., 1987; Rao et al., 2003) and now genome sequences for types 5, 14, and 15 are available (Li et al., 2006; Li et al., 2007; Tan et al., 2008).

The importance of CPV infections was first recognized in the silkworm industry, where these viruses caused economically significant losses of cocoon production (Aruga, 1963, 1971; Hukuhara, 1971; Hukuhara, 1985; Hukuhara and Midorikawa, 1983). For this reason BmCPV has been extensively studied in sericultural institutes. In *Bombyx mori* larvae, CPV primarily infects epithelial midgut cells. Late in infection, the gut becomes enlarged and milky-white in color, a result of the formation of masses of polyhedra. Ruptured cells release polyhedra into the gut lumen and these together with desquamated epithelial cells are eliminated in the feces and reach the environment. These polyhedra contaminate leaves or artificial diets and serve as a stable source of cypovirus that infect feeding larvae. Ingested polyhedra dissolve in the alkaline midgut releasing virus particles that initially infect the midgut epithelia. CPV is a unique member of the family *Reoviridae* which lacks the outer protective shells that exist in all other members, yet exhibits unusual stability and the integrity of the CPV capsids was unaffected under high-pH conditions (Zhang et al., 2002). *In vivo* entry of BmCPV into the silkworm midgut was studied by electron microscopy of ultrathin sections of midguts from silkworm larvae (Tan et al., 2003). Virions were seen adhering to the plasma membrane of microvilli, embedding in the membrane and settling themselves intact inside the microvilli of the columnar cells. These results suggested that intact virions entered columnar cells by means of direct penetration through the cell membrane.

The Virus particle

Polyhedra are easily obtained from infected larvae and virus particles purified from alkaline treated polyhedra have been investigated using a variety of analytical, enzymatic and biophysical methods. Negative stained electron microscopy revealed that cypovirus particles are ~60nm diameter spheres with 12 prominent turrets which extend ~4nm outwards from the surface at icosahedral 6-fold symmetry axes (Miura et al., 1969). The size and shape of the cypovirus particles are similar to the core particles of orthoreovirus and BTV, members of the *Reoviridae* for which atomic structures have been determined by protein X-ray crystallography (Grimes et al., 1998; Reinisch et al., 2000). SDS–PAGE analysis revealed that BmCPV virus particles contain five structural proteins VP1 (148 kDa), VP2 (136 kDa), VP3 (130 kDa), VP4 (64 kDa), and VP7 (LPP, 50kD) which are encoded by dsRNA segments 1, 2, 4, 6 and 7, respectively(Arella et al., 1988; Aruga, 1963; Hagiwara et al., 2001; Hagiwara and Matsumoto, 2000; Hagiwara et al., 2002; Hagiwara et al., 1998a; Hagiwara et al., 1998b; Ikeda et al., 2001; Mertens et al., 2004a, b; Mori et al., 1989; Mori et al., 1987; Rao et al., 2003; Zhou et al., 2003). VP1 and VP3 are major components of the capsid while VP2 is a minor capsid protein (Lewandowski and Traynor, 1972) and *in vitro* labeling of BmCPV with ^{125}I indicated that both VP1 and VP3 were outer components of the virus particle (Lewandowski and Traynor, 1972; McCrae and Mertens, 1983; Payne and Mertens, 1983). Purified CPV particles have both mRNA capping enzyme and RNA-dependent RNA polymerase enzymatic activities (Furuichi, 1974, 1978; Furuichi and Miura, 1975). The segmented dsRNA genomes are transcribed and replicated within viral capsids by the RNA-dependent RNA polymerase. VP2 and VP3 are considered to be the RNA dependent RNA polymerase and guanylyl transferase capping enzyme, respectively (Mertens et al., 2004a, b). Cypovirus proteins, protein function and corresponding dsRNA segments are tabulated at the Reoviridae Web Database (http://www.reoviridae.org).

Two groups reported the fine structure of *Orgyia pseudosugata* CPV (CPV-5) and *Dendrolimus spectabilis* (CPV-1) (Hill et al., 1999; Zhou et al., 2003), respectively. A high resolution electron density map of the BmCPV (CPV-1) particle has been recently obtained (Fig. 2A) from 12,814 cryo-EM images of individual particles using icosahedral symmetry to combine these multiple images into a single three-dimensional icosahedrally averaged electron density map (Yu et al., 2008; Zhou, 2008a; Zhou, 2008b). The 3.88Å resolution obtained was sufficient to allow a tentative alignment of some protein amino-acid sequences into the electron density map. In particular, the positions of the C-alpha atoms for 70% of VP1 and for 33% of VP3 have been deposited at the protein data bank (code 3CNF). The icosahedral subunit consists of two VP1 molecules with different conformations (CSP-A and CSP-B), two VP7 molecules with different conformations (LPP-3 and LPP-5) and a single VP3 molecule (the turret protein TP). The virus particle consists of 60 these icosahedral subunits together with components that do not have icosahedral symmetry – e.g. the dsRNA molecules and the 'A spikes', fibrous molecules extending from the centre of each of the 12 turrets. Protein density corresponding to the CSP-A, CSP-B, the two LPP conformers and two N-terminal domains of TP could be identified in the map, which also revealed averaged out density corresponding to the A-spike and outer parts of the dsRNA genome.

Consistent with the overall structural similarity of cypovirus with the orthoreovirus core, VP1 has a similar fold and secondary structure elements as the corresponding reovirus protein lambda 1, with the two molecules with different conformations CSP-A and CSP-B together forming a connected thin plate shell for the particle. An exception to this overall structural homology is the small protrusion domain (SPP), unique to VP1. Two non-equivalent VP7 molecules (reovirus sigma 2 homologs) close the VP1 shell forming clamps near the 3-fold (LPP-3) and 5-fold (LPP-5) symmetry axes. Each turret is formed from 5 equivalent VP3 (TP) molecules. A unique feature of cypovirus is a cleft at the base of

the turret, formed by apical domains of two CSP-As and one CSP-B and proposed to be the exit channel for nascent mRNAs because it is adjacent to the guanyltransferase active site of VP3. The turret protein VP3 has a similar overall domain architecture to the orthoreovirus equivalent lambda 2, but lacks the immunoglobulin fold flap domain, and instead forms a hollow pentameric structure with the central chamber plugged by the A-spike protein. The N-terminal 79 amino-acids of VP3 form a separate domain, also unique to cypovirus, which extends outwards from the base of the turret (Fig. 2B). This largely beta-strand domain corresponds to the minimal N-terminal region of VP3 used to target foreign proteins into recombinant cypovirus polyhedra (Ikeda et al., 2006) and for that reason has been termed the polyhedrin binding domain (Yu et al., 2008).

Polyhedra

The matrix protein of BmCPV polyhedra is called polyhedrin and encoded by the smallest segment 10 (Arella et al., 1988; Ikeda et al., 1998; Mori et al., 1993; Mori et al., 1989; Mori et al., 1987; Nakazawa et al., 1996). The BmCPV polyhedrin gene consists of 944 base pairs encoding a polypeptide of 248 amino acids with predicted molecular mass ~29 kDa. Many BmCPV strains have been isolated according to the shape and localization of the polyhedra (Hukuhara, 1971; Hukuhara, 1985; Hukuhara and Midorikawa, 1983). The polyhedrin gene from wild-type isolate (strain H) was introduced into a baculovirus expression vector and the insect cell line *Spodoptera frugiperda* IPLB-Sf21AE (Sf cells) was infected with the recombinant baculovirus designated AcCP-H. The polyhedrin of strain H was massively produced and many cubic polyhedra were observed in Sf cells (Mori et al., 1993) (Fig. 1B). This result demonstrated that other cypovirus-encoded proteins were unnecessary for the crystallization of BmCPV polyhedrin.

Polyhedra function to facilitate the survival of the virus in the environment, stabilizing the

virus particles and allowing them to remain viable for long periods (Belloncik, 1989; Belloncik and Mori, 1998; Hukuhara and Bohami, 1991; Payne and Mertens, 1983). Polyhedra are remarkably stable under physiological conditions, but do dissolve at pH > 10.5. Infection occurs by the release of the virus particles in the alkaline larval midgut after ingestion. Only three virus families, all from insects, share this mode of propagation within infectious protein crystals. Besides cypovirus, DNA viruses in the baculovirus group (nucleopolyhedrovirus and granulovirus) and the entomopoxvirus group (Rohrmann, 1986) also produce polyhedra. Baculovirus polyhedrin has a molecular weight similar to CPV polyhedrin; however, there is no homology between the amino acid sequences of the two types of polyhedrin. Baculovirus polyhedra incorporate fewer virus particles than cypovirus polyhedra, which each occlude thousands of virus particles as they grow in the cytoplasm of infected cells (Belloncik, 1989; Belloncik and Mori, 1998; Payne and Mertens, 1983). The maintenance of occlusion body proteins in such a diverse group of viruses indicates the importance of polyhedrin in the life cycles of these insect viruses.

The atomic structure of BmCPV polyhedra from a wild-type strain has been determined to a resolution of 2Å (Coulibaly et al., 2007). The crystals have body centered cubic symmetry with a 103Å unit cell, the same symmetry and unit cell as baculovirus polyhedra, but a different underlying protein structure (Coulibaly et al., 2009; Ji et al., 2010). Each unit cell contains 24 identical polyhedrin molecules in different positions and orientations related by I23 space group symmetry. A typical 2-micron crystal contains about 200 million polyhedrin molecules, 8 million cubic unit cells and thousands of virus particles. The virus particles within polyhedra each displace approximately 200 unit cells from the crystalline polyhedrin lattice. The proportion of the volume occupied by virus particles in a 2-micron crystal containing 1000 particles is 2.5%.

The atomic structure revealed that cypovirus polyhedra are extraordinarily intricate and

densely packed, unlike laboratory crystallized proteins where only a tiny fraction of the surface area of each molecule in the crystal interacts with other molecules. Analysis of all the contacts to other molecules in polyhedra revealed that the strongest crystalline interactions formed trimers of molecules within the crystal. For this reason, the structure of polyhedra is conveniently described as being based on trimeric building blocks (although all the molecules in the crystal are identical). Individual polyhedrin molecules have a distinctive extended N-terminal α helix (the H1 helix) which projects from the main part of the molecule, a compact β sandwich domain with 3 layered β sheets and peripheral small α helices (Fig. 3A). The trimeric building blocks are linked to each other in polyhedra by multiple interactions, primarily involving these extended H1 N-terminal arms. The trimers themselves are formed by extensive hydrophobic interactions between monomers, particularly between the H4 helices which surround the three-fold axis (Fig. 3B, C). The trimeric building blocks may represent an assembly intermediate for polyhedra, but this is yet to be determined.

Polyhedra are stable in reagents that would normally be expected to denature proteins (concentrated urea, SDS, acid etc.). The structure is consistent with this, with numerous protein-protein contacts shielding over 70% of the monomer surface from solvent. Polyhedra do however dissolve readily above 10.5 and the deprotonation of a cluster of buried cluster of tyrosines (pKa ~10.1) may provide a clue for the disassembly mechanism. Larval alkaline proteinases degrade polyhedrin further contributing to the efficient release of virus from polyhedra in the mid-gut (Coulibaly et al., 2007).

The nucleotides ATP, GTP and CTP were identified in cypovirus polyhedra by mass-spectrometry and the structure revealed a single molecule of each nucleotide bound to each polyhedrin molecule. The ATP and GTP molecules are bound at the interface between four trimers and the CTP molecule is located near the central cavity (Coulibaly et al., 2007).

The function of the bound nucleotides is unknown. No other adducts, other than virus particles, have been discovered within polyhedra.

Incorporation of cypovirus particles into polyhedra

In the case of baculovirus, it has been hypothesized that virus particle occlusion and polyhedral growth are initiated by specific interactions between polyhedrin molecules and the virus particle envelope(Eason et al., 1998). For cypovirus, similar specific interactions between CPV polyhedrin and a viral capsid protein may lead to occlusion of virus particles into polyhedra. Iodination of BmCPV virus particle and analysis of the labeled polypeptides by SDS-PAGE first indicated that VP1 and VP3 are outer components of the BmCPV particle(Lewandowski and Traynor, 1972; McCrae and Mertens, 1983). VP3 was first selected to investigate interaction with BmCPV polyhedrin in the occlusion of virus particles into the polyhedra (Ikeda et al., 2001). Green fluorescent protein (GFP) was fused to the C-terminus of BmCPV VP3 and introduced into the baculovirus expression vector, resulting in AcVP3/GFP (Ikeda et al., 2001). The fusion protein of VP3 and GFP was co-expressed with AcCP-H polyhedrin in Sf21 cells. The polyhedra were purified and green fluorescence observed under UV irradiation. The fluorescence indicated that the VP3-GFP chimera was incorporated into these polyhedra (Fig. 4). The fluorescence disappeared when the polyhedra were suspended in acetate buffer at pH 4 and reappeared after the pH was increased. There was no change in the appearance of BmCPV polyhedra produced by AcCP-H below pH 10, however, when the pH increased above 10, the polyhedra dissolved rapidly and the green fluorescence was intensified (Ikeda et al., 2001). This effect could be due to the release of the VP3-GFP chimera from the dissolving polyhedra. No fluorescence was detected in polyhedra obtained from cells infected with both AcGFP and AcCP-H, indicating that the chimeric protein occlusion was initiated by specific interactions between BmCPV polyhedrin and

VP3(Ikeda et al., 2001).

In order to map an immobilization signal to a fragment of the BmCPV VP3 protein, either the N-terminal or C-terminal half of VP3 was fused to the N-terminus of EGFP and recombinant baculoviruses encoding these two chimeric proteins were constructed (Ikeda et al., 2006). One of these viruses, designated AcVP3(N)/GFP, encoded amino acids 1-448 of VP3 fused to EGFP and the other, designated AcGFP/VP3(C), encoded EGFP fused to amino acids 428-1057 of VP3. Each recombinant virus was used for double infections together with AcCP-H, which is a third recombinant that produces a cubic form of BmCPV polyhedra. Green fluorescence was observed, predominantly on the surface, with polyhedra isolated from cells that had been co-infected with AcVP3 (N)/GFP and AcCP-H (Ikeda et al., 2006). In contrast, no green fluorescence was observed with polyhedra isolated from cells that had been co-infected with AcGFP/VP3(C) and AcCP-H.

A large number of recombinant baculoviruses encoding different VP3-GFP fusion proteins were subsequently constructed to identify the minimal region of VP3 required to target the GFP fusion construct to polyhedra. Sf cells were co-infected with these recombinant baculoviruses and AcCP-H, polyhedra were purified from each doubly-infected culture, and then the presence of each fusion protein in the polyhedra was determined by confocal microscopy. Based upon the results of these analyses, it was concluded that the occlusion of GFP into polyhedra required the region of VP3 between amino acids 1 and 79 and this amino acid sequence also was able to direct the immobilization of other foreign proteins into polyhedra (Ikeda et al., 2006). VP3 is the turret protein (TP) of BmCPV and the N-terminal 79 residues form a separate domain on the outside of the turret (Yu et al., 2008). The N-terminal 79 residues of VP3 were named the immobilization signal (Ikeda et al., 2006) or polyhedrin-binding domain (PBD) (Yu et al., 2008), since these residues form a separate domain at the base of the turret, as seen in the 3.88Å resolution cryo-EM map (Yu et al.,

2008).

Polyhedra as protein nanocontainers

The atomic structure of BmCPV polyhedra revealed trimeric building blocks connected by extensive interactions, many involving the polyhedrin H1 helix (Coulibaly et al., 2007). Each building block consists of a cluster of three identical polyhedrin molecules and the three corresponding N-terminal H1 helices project outwards from the centre of the trimer. The building blocks are interlocked with other identical building blocks to form a tight scaffold largely generated by H1-helix (Coulibaly et al., 2007). Because the H1 helix is at the N-terminus of the molecule and projects outwards from the structure it may form into a helix independently as the molecule folds. This possibility, together with its role in cross-linking polyhedra, led to the suggestion that the polyhedrin H1 helix might also prove to be a useful tag for incorporating foreign proteins into polyhedra, like the VP3 residue 1-79 imobilization signal.

The H1-helix sequence was added to either the N-terminus or the C-terminus of enhanced green fluorescent protein (EGFP). Each recombinant EGFP (H1/EGFP and EGFP/H1) was co-expressed with BmCPV polyhedrin using the baculovirus expression vector system. Immobilization of EGFP fused with H1 signal was compared with VP3 signal. The emission of green fluorescence from H1/EGFP polyhedra displayed a greater intensity compared than either EGFP/H1 and EGFP/VP3 polyhedra (Fig. 4). The VP3 signal and the H1signal were used together to produce polyhedra containing both EGFP and DsRed. EGFP and DsRed were fused with VP3 signal (EGFP/VP3) and H1 signal (H1/DsRed), respectively, and the reverse conformations (H1/EGFP and DsRed/VP3) were also constructed (Fig. 5). The double-labeled polyhedra with EGFP and DsRed were isolated and imaged using dual wavelength confocal fluorescence microscopy, showing that a multiple proteins can be

incorporated into single polyhedra using both VP3 and H1 immobilization signals.

The encapsulations of fibroblast growth factor-2 (FGF-2) and FGF-7, epidermal growth factor (EGF), leukemia inhibitory factor, and secreted frizzled-related protein 4 into polyhedra have been reported (Ijiri et al., 2009; Matsushima et al., 2010; Mori et al., 2007; Nishishita et al., 2011). These cytokines have biological activities as monomers. The vascular endothelial growth factor (VEGF) family plays an integral role in angiogenesis, lymphangiogenesis, and vasculogenesis (Ferrara, 2004; Hoeben et al., 2004). The VEGF family currently comprises seven members (VEGF-A, VEGF-B, VEGF-C, VEGF-D, VEGF-E, VEGF-F, and placental growth factor). All members have a common VEGF homology domain. The core region is composed of a cysteine knot motif, with eight invariant cysteine residues involved in inter- and intramolecular disulfide bonds at one end of a conserved central four-stranded β-sheet within each monomer, which dimerize in an antiparallel, side-by-side orientation (Ferrara, 2004; Hoeben et al., 2004; Neufeld et al., 1999; Ortega et al., 1999). VEGF-A is a 34- to 42-kDa, dimeric, disulfide-bound glycoprotein. VEGF-A exists in at least seven homodimeric isoforms where each subunit consists of 121, 145, 148, 165, 183, 189, or 206 amino acids (Ferrara, 2004; Hoeben et al., 2004). Before the encapsulation of VEGF-A into polyhedra, overexpression of protein disulfide bond isomerase (PDI) is required to obtain biologically active VEGF-encapsulated polyhedra.

Bone morphogenetic protein (BMP) is a member of the transforming growth factor-β (TGF-β) superfamily and is also a disulfide-linked homodimer that induces bone and cartilage formation. BMP-2 has been shown to induce new bone formation in animal models and is now well recognized as one of the key osteogenic factors in the field of bone-tissue engineering (Reddi, 1994, 1997; Schmitt et al., 1999). BMP-2 induces bone regeneration in fracture healing by activating a set of cellular events including chemotaxis of uncommitted mesenchymal cells and differentiation of these cells into osteoblasts (Fiedler et al., 2002;

Mont et al., 2004).

Endostatin, a 20-kDa C-terminal fragment digested from collagen XVIII, inhibits the proliferation and migration of endothelial cells, and induces apoptosis, leading to repression of growth of a wide variety of tumors with neovascularization (Folkman, 2006; O'Reilly et al., 1997). The apoptotic effect of endostatin is associated with decreased levels of anti-apoptotic molecules (Dixelius et al., 2000). Recently, Zhuo *et al.* reported that endostatin directly inhibits lymphatic endothelial cells (LEC) and lymphangiogenic vessels via the cell surface receptor nucleolin on LEC which inhibits lymphatic metastasis (Zhuo et al., 2010).

In this study VEGF, endostatin, and BMP-2 were encapsulated into polyhedra. In chapter 2, the effect of both VEGF and endostatin polyhedra on angiogenesis in cell culture and *in vivo* was investigated. In chapter 3 it was also showed that BMP-2 encapsulated polyhedra induced new bone more effectively than collagen-BMP-2 protein complexes when tested *in vivo*. In chapter 4, I evaluated FGF-2 polyhedra and FGF-7 polyhedra for activity in 3D cell cultures of keratinocytes and melanocytes. Furthermore, the cytoprotective effects of FGF-7 polyhedra on keratinocytes exposed to reactive oxygen species (ROS) were investigated.

References

Arella, M., Lavallee, C., Belloncik, S., and Furuichi, Y. (1988). Molecular cloning and characterization of cytoplasmic polyhedrosis virus polyhedrin and a viable deletion mutant gene. J Virol *62*, 211-217.

Aruga, H. (1963). Induction of virus infection. In An Advence Treatise, E.A. Steinhaus, ed. (New York, Academic Press), pp. 499-530.

Aruga, H. (1971). Cytoplasmic polyhedrosis of the silkworm—Historical, economical and epizootiological aspects. In The Cytoplasmic Polyhedrosis Virus of the Silkworm, H. Aruga, and Y. Tanada, eds. (Tokyo, University of Tokyo Press), pp. 3-57.

Belloncik, S. (1989). Cytoplasmic polyhedrosis viruses-Reoviridae. Adv Virus Res *37*, 173-209.

Belloncik, S., and Mori, H. (1998). Cypovirus. In The insect viruses, L.K. Miller, and L.A. Ball, eds. (New York, Plenum Press), pp. 337-369.

Coulibaly, F., Chiu, E., Gutmann, S., Rajendran, C., Haebel, P.W., Ikeda, K., Mori, H., Ward, V.K., Schulze-Briese, C., and Metcalf, P. (2009). The atomic structure of baculovirus polyhedra reveals the independent emergence of infectious crystals in DNA and RNA viruses. Proc Natl Acad Sci U S A *106*, 22205-22210.

Coulibaly, F., Chiu, E., Ikeda, K., Gutmann, S., Haebel, P.W., Schulze-Briese, C., Mori, H., and Metcalf, P. (2007). The molecular organization of cypovirus polyhedra. Nature *446*, 97-101.

Dixelius, J., Larsson, H., Sasaki, T., Holmqvist, K., Lu, L., Engstrom, A., Timpl, R., Welsh, M., and Claesson-Welsh, L. (2000). Endostatin-induced tyrosine kinase signaling through the Shb adaptor protein regulates endothelial cell apoptosis. Blood *95*, 3403-3411.

Eason, J.E., Hice, R.H., Johnson, J.J., and Federici, B.A. (1998). Effects of substituting granulin or a granulin-polyhedrin chimera for polyhedrin on virion occlusion and polyhedral morphology in Autographa californica multinucleocapsid nuclear polyhedrosis virus. J Virol *72*, 6237-6243.

Ferrara, N. (2004). Vascular endothelial growth factor: basic science and clinical progress. Endocr Rev *25*, 581-611.

Fiedler, J., Roderer, G., Gunther, K.P., and Brenner, R.E. (2002). BMP-2, BMP-4, and PDGF-bb stimulate chemotactic migration of primary human mesenchymal progenitor cells. J Cell Biochem *87*, 305-312.

Folkman, J. (2006). Antiangiogenesis in cancer therapy--endostatin and its mechanisms of action. Exp Cell Res *312*, 594-607.

Furuichi, Y. (1974). "Methylation-coupled" transcription by virus-associated transcriptase of cytoplasmic polyhedrosis virus containing double-stranded RNA. Nucleic Acids Res *1*, 809-822.

Furuichi, Y. (1978). "Pretranscriptional capping" in the biosynthesis of cytoplasmic polyhedrosis virus mRNA. Proc Natl Acad Sci U S A *75*, 1086-1090.

Furuichi, Y., and Miura, K. (1975). A blocked structure at the 5' terminus of mRNA from cytoplasmic polyhedrosis virus. Nature *253*, 374-375.

Graham, R.I., Rao, S., Possee, R.D., Sait, S.M., Mertens, P.P., and Hails, R.S. (2006). Detection and characterisation of three novel species of reovirus (Reoviridae), isolated from geographically separate populations of the winter moth Operophtera brumata (Lepidoptera: Geometridae) on Orkney. J Invertebr Pathol *91*, 79-87.

Grimes, J.M., Burroughs, J.N., Gouet, P., Diprose, J.M., Malby, R., Zientara, S., Mertens, P.P., and Stuart, D.I. (1998). The atomic structure of the bluetongue virus core. Nature *395*, 470-478.

Hagiwara, K., Kobayashi, J., Tomita, M., and Yoshimura, T. (2001). Nucleotide sequence of genome segment 5 from Bombyx mori cypovirus 1. Arch Virol *146*, 181-187.

Hagiwara, K., and Matsumoto, T. (2000). Nucleotide sequences of genome segments 6 and 7 of Bombyx mori cypovirus 1, encoding the viral structural proteins V4 and V5, respectively. J Gen Virol *81*, 1143-1147.

Hagiwara, K., Rao, S., Scott, S.W., and Carner, G.R. (2002). Nucleotide sequences of segments 1, 3 and 4 of the genome of Bombyx mori cypovirus 1 encoding putative capsid proteins VP1, VP3 and VP4, respectively. J Gen Virol *83*, 1477-1482.

Hagiwara, K., Tomita, M., Kobayashi, J., Miyajima, S., and Yoshimura, T. (1998a). Nucleotide sequence of Bombyx mori cytoplasmic polyhedrosis virus segment 8. Biochem Biophys Res Commun *247*, 549-553.

Hagiwara, K., Tomita, M., Nakai, K., Kobayashi, J., Miyajima, S., and Yoshimura, T. (1998b). Determination of the nucleotide sequence of Bombyx mori cytoplasmic polyhedrosis virus segment 9 and its expression in BmN4 cells. J Virol *72*, 5762-5768.

Hill, C.L., Booth, T.F., Prasad, B.V., Grimes, J.M., Mertens, P.P., Sutton, G.C., and Stuart, D.I. (1999). The structure of a cypovirus and the functional organization of dsRNA viruses. Nat Struct Biol *6*, 565-568.

Hoeben, A., Landuyt, B., Highley, M.S., Wildiers, H., Van Oosterom, A.T., and De Bruijn, E.A. (2004). Vascular endothelial growth factor and angiogenesis. Pharmacol Rev *56*, 549-580.

Hukuhara, T. (1971). Variations in cytoplasmic-polyhedrosis virus. In The Cytoplasmic Polyhedrosis of the Silkworm, H. Aruga, and Y. Tanada, eds. (Tokyo, University of Tokyo Press), pp. 79-100.

Hukuhara, T. (1985). Pathology associated with cytoplasmic polyhedrosis viruses. In Viral Insecticides for Biological Control, H. Aruga, and Y. Tanada, eds. (New York, Academic Press), pp. 121-161.

Hukuhara, T., and Bohami, J.R. (1991). Reoviridae. In Atlas of Invertebrate Viruses, J.R. Adams, and J.R. Bohami, eds. (BocaRaton,Fla, CRC Press), pp. 393-434.

Hukuhara, T., and Midorikawa, M. (1983). Pathogenesis of cytoplasmic polyhedrosis in the silkworm. In Double-Stranded RNA Viruses, R.W. Compans, and D.H.L. Bishop, eds. (New York, Elsevier Biomedical), pp. 405-414.

Ijiri, H., Coulibaly, F., Nishimura, G., Nakai, D., Chiu, E., Takenaka, C., Ikeda, K., Nakazawa, H., Hamada, N., Kotani, E., *et al.* (2009). Structure-based targeting of bioactive proteins into cypovirus polyhedra and application to immobilized cytokines for mammalian cell culture. Biomaterials *30*, 4297-4308.

Ikeda, K., Nagaoka, S., Winkler, S., Kotani, K., Yagi, H., Nakanishi, K., Miyajima, S.,

Kobayashi, J., and Mori, H. (2001). Molecular characterization of Bombyx mori cytoplasmic polyhedrosis virus genome segment 4. J Virol *75*, 988-995.

Ikeda, K., Nakazawa, H., Alain, R., Belloncik, S., and Mori, H. (1998). Characterizations of natural and induced polyhedrin gene mutants of Bombyx mori cytoplasmic polyhedrosis viruses. Arch Virol *143*, 241-248.

Ikeda, K., Nakazawa, H., Shimo-Oka, A., Ishio, K., Miyata, S., Hosokawa, Y., Matsumura, S., Masuhara, H., Belloncik, S., Alain, R., *et al.* (2006). Immobilization of diverse foreign proteins in viral polyhedra and potential application for protein microarrays. Proteomics *6*, 54-66.

Ji, X., Sutton, G., Evans, G., Axford, D., Owen, R., and Stuart, D.I. (2010). How baculovirus polyhedra fit square pegs into round holes to robustly package viruses. EMBO J *29*, 505-514.

Lewandowski, L.J., and Traynor, B.L. (1972). Comparison of the structure and polypeptide composition of three double-stranded ribonucleic acid-containing viruses (diplornaviruses): cytoplasmic polyhedrosis virus, wound tumor virus, and reovirus. J Virol *10*, 1053-1070.

Li, Y., Tan, L., Chen, W., Zhang, J., and Hu, Y. (2006). Identification and genome characterization of Heliothis armigera cypovirus types 5 and 14 and Heliothis assulta cypovirus type 14. J Gen Virol *87*, 387-394.

Li, Y., Zhang, J., Tan, L., Chen, W., Luo, H., and Hu, Y. (2007). Phylogenetic analysis of Heliothis armigera cytoplasmic polyhedrosis virus type 14 and a series of dwarf segments found in the genome. J Gen Virol *88*, 991-997.

Matsushima, K., Suyama, T., Takenaka, C., Nishishita, N., Ikeda, K., Ikada, Y., Sawa, Y., Jakt, L.M., Mori, H., and Kawamata, S. (2010). Secreted frizzled related protein 4 reduces fibrosis scar size and ameliorates cardiac function after ischemic injury. Tissue Eng Part A *16*, 3329-3341.

McCrae, M.A., and Mertens, P.P.C. (1983). In vitro translation studies on and RNA coding

assignments for cytoplasmic polyhedrosis viruses. In Double-Stranded RNA Viruses, R.W. Compans, and D.H.L. Bishop, eds. (New York, Elsevier Biomedical), pp. 35-41.

Mertens, P.P.C., Rao, S., and Zhou, H. (2004a). Cypovirus. In Virus taxonomy: eighth report of the International Committee on Taxonomy of Viruses, C.M. Fauquet, M.A. Mayo, J. Maniloff, U. Desselberger, and L.A. Ball, eds. (London England, Elsevier Academic Press), pp. 522–533.

Mertens, P.P.C., Rao, S., and Zhou, H. (2004b). Reoviridae. In Virus taxonomy: eighth report of the International Committee on Taxonomy of Viruses, C.M. Fauquet, M.A. Mayo, J. Maniloff, U. Desselberger, and L.A. Ball, eds. (London England, Elsevier Academic Press), pp. 447–454.

Miura, K., Fujii-Kawata, I., Iwata, H., and Kawase, S. (1969). Electron-microscopic observation of a cytoplasmic-polyhedrosis virus from the silkworm. Journal of Invertebrate Pathology *14*, 262-265.

Mont, M.A., Ragland, P.S., Biggins, B., Friedlaender, G., Patel, T., Cook, S., Etienne, G., Shimmin, A., Kildey, R., Rueger, D.C.*, et al.* (2004). Use of bone morphogenetic proteins for musculoskeletal applications. An overview. J Bone Joint Surg Am *86-A Suppl 2*, 41-55.

Mori, H., Ito, R., Nakazawa, H., Sumida, M., Matsubara, F., and Minobe, Y. (1993). Expression of Bombyx mori cytoplasmic polyhedrosis virus polyhedrin in insect cells by using a baculovirus expression vector, and its assembly into polyhedra. J Gen Virol *74 (Pt 1)*, 99-102.

Mori, H., Minobe, Y., Sasaki, T., and Kawase, S. (1989). Nucleotide sequence of the polyhedrin gene of Bombyx mori cytoplasmic polyhedrosis virus A strain with nuclear localization of polyhedra. J Gen Virol *70 (Pt 7)*, 1885-1888.

Mori, H., Sasaki, T., Minobe, Y., Miyajima, S., and Kawase, S. (1987). Difference of proteins from inclusion bodies formed in the nucleus and cytoplasm of the cytoplasmic

polyhedrosis virus infected midgut in the silkworm, Bombyx mori. Journal of Invertebrate Pathology *50*, 26-32.

Mori, H., Shukunami, C., Furuyama, A., Notsu, H., Nishizaki, Y., and Hiraki, Y. (2007). Immobilization of bioactive fibroblast growth factor-2 into cubic proteinous microcrystals (Bombyx mori cypovirus polyhedra) that are insoluble in a physiological cellular environment. J Biol Chem *282*, 17289-17296.

Nakazawa, H., Kendirgi, F., Belloncik, S., Ito, R., Takagi, S., Minobe, Y., Higo, K., Sumida, M., Matsubara, F., and Mori, H. (1996). Effect of mutations on the intracellular localization of Bombyx mori cytoplasmic polyhedrosis virus polyhedrin. J Gen Virol *77 (Pt 1)*, 147-153.

Neufeld, G., Cohen, T., Gengrinovitch, S., and Poltorak, Z. (1999). Vascular endothelial growth factor (VEGF) and its receptors. FASEB J *13*, 9-22.

Nishishita, N., Ijiri, H., Takenaka, C., Kobayashi, K., Goto, K., Kotani, E., Itoh, T., Mori, H., and Kawamata, S. (2011). The use of leukemia inhibitory factor immobilized on virus-derived polyhedra to support the proliferation of mouse embryonic and induced pluripotent stem cells. Biomaterials *32*, 3555-3563.

O'Reilly, M.S., Boehm, T., Shing, Y., Fukai, N., Vasios, G., Lane, W.S., Flynn, E., Birkhead, J.R., Olsen, B.R., and Folkman, J. (1997). Endostatin: an endogenous inhibitor of angiogenesis and tumor growth. Cell *88*, 277-285.

Ortega, N., Hutchings, H., and Plouet, J. (1999). Signal relays in the VEGF system. Front Biosci *4*, D141-152.

Payne, C.C., and Mertens, P.P.C. (1983). Cytoplasmic Polyhedrosis Viruses. In The Reoviridae, W.K. Joklik, ed. (New York, Plenum), pp. 425-504.

Rao, S., Carner, G.R., Scott, S.W., Omura, T., and Hagiwara, K. (2003). Comparison of the amino acid sequences of RNA-dependent RNA polymerases of cypoviruses in the family Reoviridae. Arch Virol *148*, 209-219.

Reddi, A.H. (1994). Symbiosis of biotechnology and biomaterials: applications in tissue engineering of bone and cartilage. J Cell Biochem *56*, 192-195.

Reddi, A.H. (1997). BMPs: actions in flesh and bone. Nat Med *3*, 837-839.

Reinisch, K.M., Nibert, M.L., and Harrison, S.C. (2000). Structure of the reovirus core at 3.6 A resolution. Nature *404*, 960-967.

Rohrmann, G.F. (1986). Polyhedrin structure. J Gen Virol *67 (Pt 8)*, 1499-1513.

Schmitt, J.M., Hwang, K., Winn, S.R., and Hollinger, J.O. (1999). Bone morphogenetic proteins: an update on basic biology and clinical relevance. J Orthop Res *17*, 269-278.

Shapiro, A., Green, T., Rao, S., White, S., Carner, G., Mertens, P.P., and Becnel, J.J. (2005). Morphological and molecular characterization of a Cypovirus (Reoviridae) from the mosquito Uranotaenia sapphirina (Diptera: Culicidae). J Virol *79*, 9430-9438.

Tan, L., Zhang, J., Li, Y., Jiang, H., Cao, X., and Hu, Y. (2008). The complete nucleotide sequence of the type 5 Helicoverpa armigera cytoplasmic polyhedrosis virus genome. Virus Genes *36*, 587-593.

Tan, Y.R., Sun, J.C., Lu, X.Y., Su, D.M., and Zhang, J.Q. (2003). Entry of Bombyx mori cypovirus 1 into midgut cells in vivo. J Electron Microsc (Tokyo) *52*, 485-489.

Yu, X., Jin, L., and Zhou, Z.H. (2008). 3.88 A structure of cytoplasmic polyhedrosis virus by cryo-electron microscopy. Nature *453*, 415-419.

Zhang, H., Yu, X.K., Lu, X.Y., Zhang, J.Q., and Zhou, Z.H. (2002). Molecular interactions and viral stability revealed by structural analyses of chemically treated cypovirus capsids. Virology *298*, 45-52.

Zhou, Z.H. (2008a). Towards atomic resolution structural determination by single-particle cryo-electron microscopy. Curr Opin Struct Biol *18*, 218-228.

Zhou, Z.H., Zhang, H., Jakana, J., Lu, X.Y., and Zhang, J.Q. (2003). Cytoplasmic polyhedrosis virus structure at 8 A by electron cryomicroscopy: structural basis of capsid

stability and mRNA processing regulation. Structure *11*, 651-663.

Zhou, Z.H.b. (2008b). Cypovirus, in Segmented Double-Stranded RNA Viruses In Structure and Molecular Biology, J.T. Patton, ed. (Norfolk, UK, Caister Academic Press), pp. 27-43. .

Zhuo, W., Luo, C., Wang, X., Song, X., Fu, Y., and Luo, Y. (2010). Endostatin inhibits tumour lymphangiogenesis and lymphatic metastasis via cell surface nucleolin on lymphangiogenic endothelial cells. J Pathol *222*, 249-260.

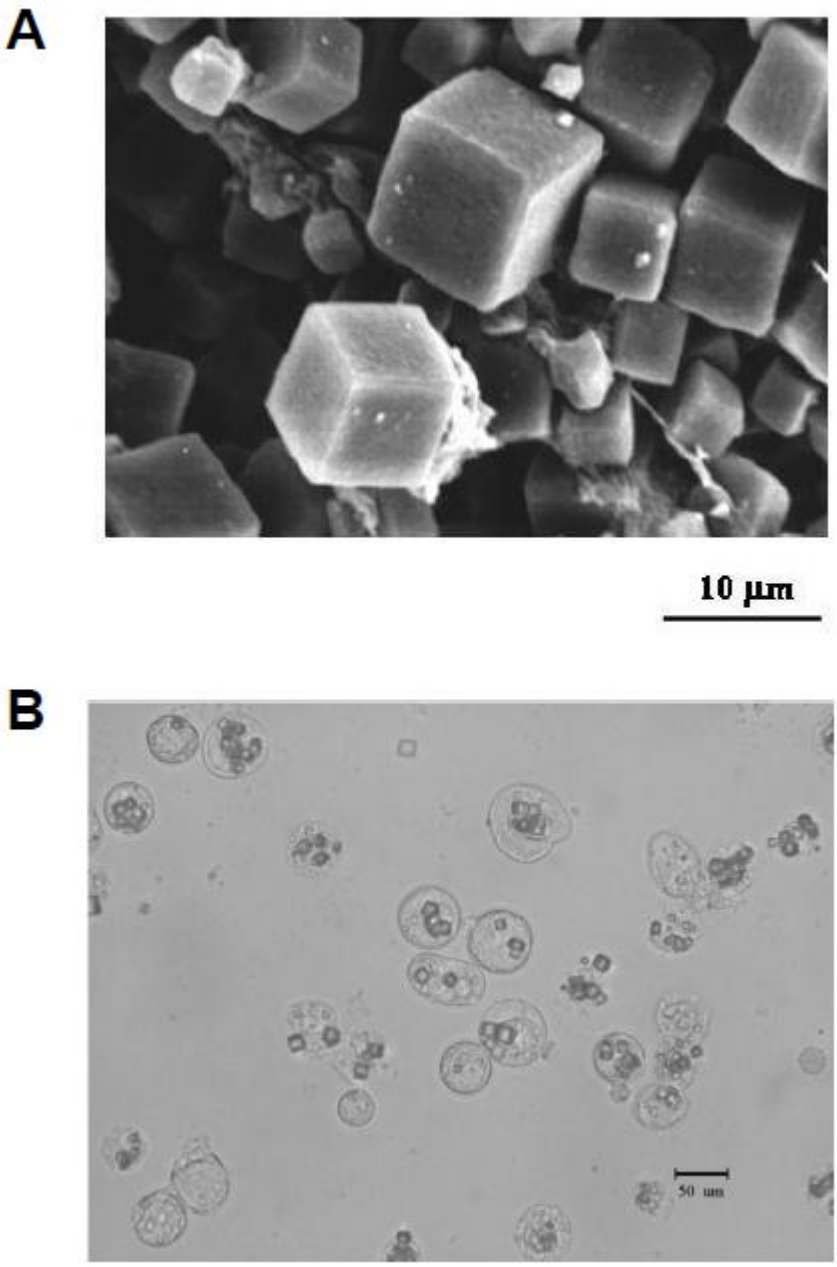

Fig. 1 BmCPV polyhedra. (A) Scanning electron micrograph of BmCPV polyhedra purified from the midgut of the silkworm. (B) Polyhedra produced by a recombinant baculovirus (AcCP-H) expressing the BmCPV polyhedrin.

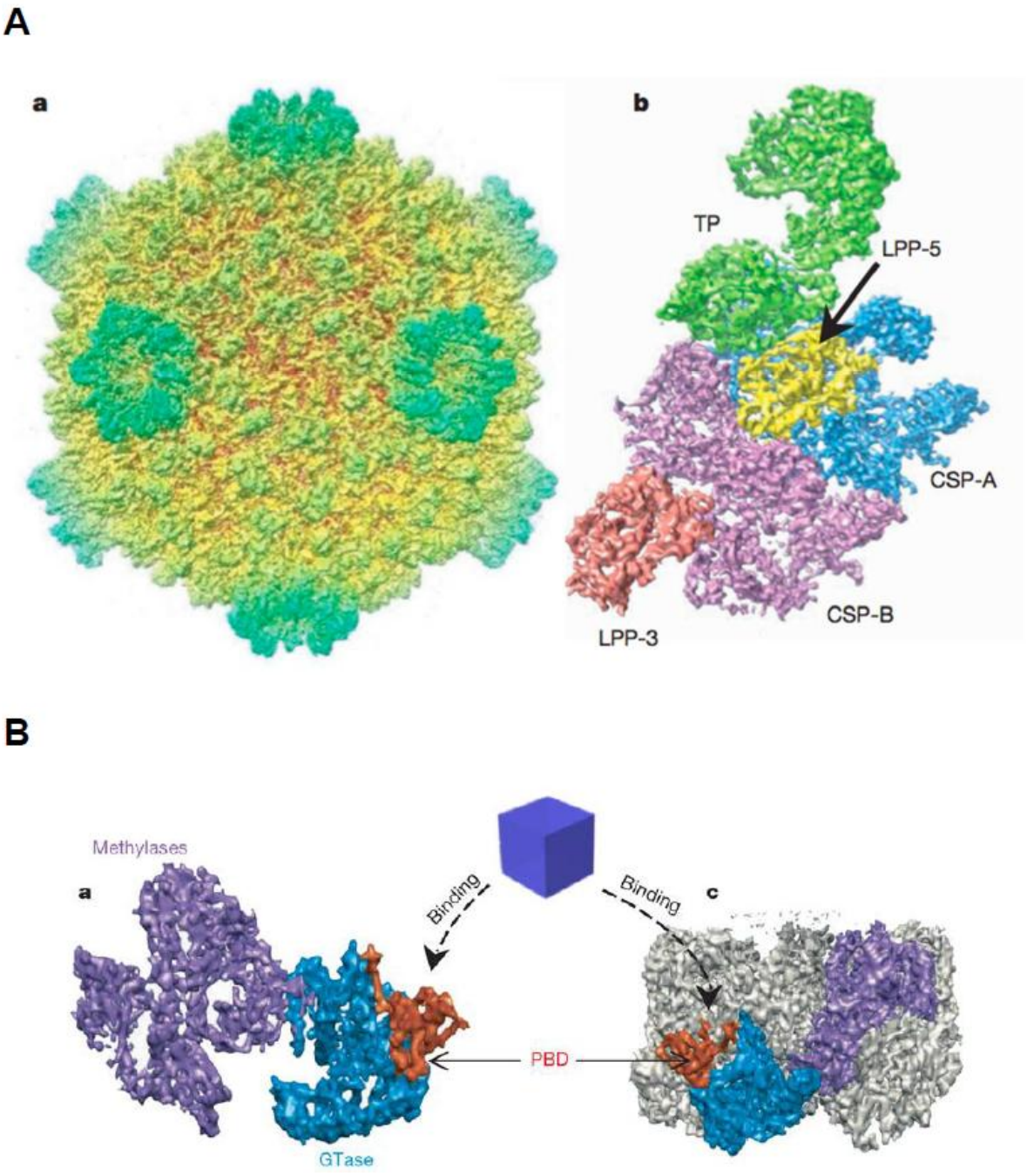

Fig. 2 BmCPV 3.88Å resolution electron density map derived from 12,814 cryo-electron microscopy single particle images using icosahedral averaging. (A) (a) The whole particle viewed down a two-fold symmetry axis. Eight of the twelve turret projects are visible in this orientation. The colours correspond to radial distance. (b) The icosahedral asymmetric unit, which is repeated 60 times to generate the whole particle. The asymmetric unit contains one TP molecule, 2 CSP molecules (CSP-A and CSP-B) and 2 LPP molecules (LPP-3 and LPP-5). (B) Turret protein (TP, VP3) electron density. (a) A single TP protein, showing the GTase and methylase domains. (b) Turret (like the 8 turrets visible in A) containing 5 TP proteins. The location of the N-terminal 79 residue polyhedrin binding domain (PBD) is indicated.

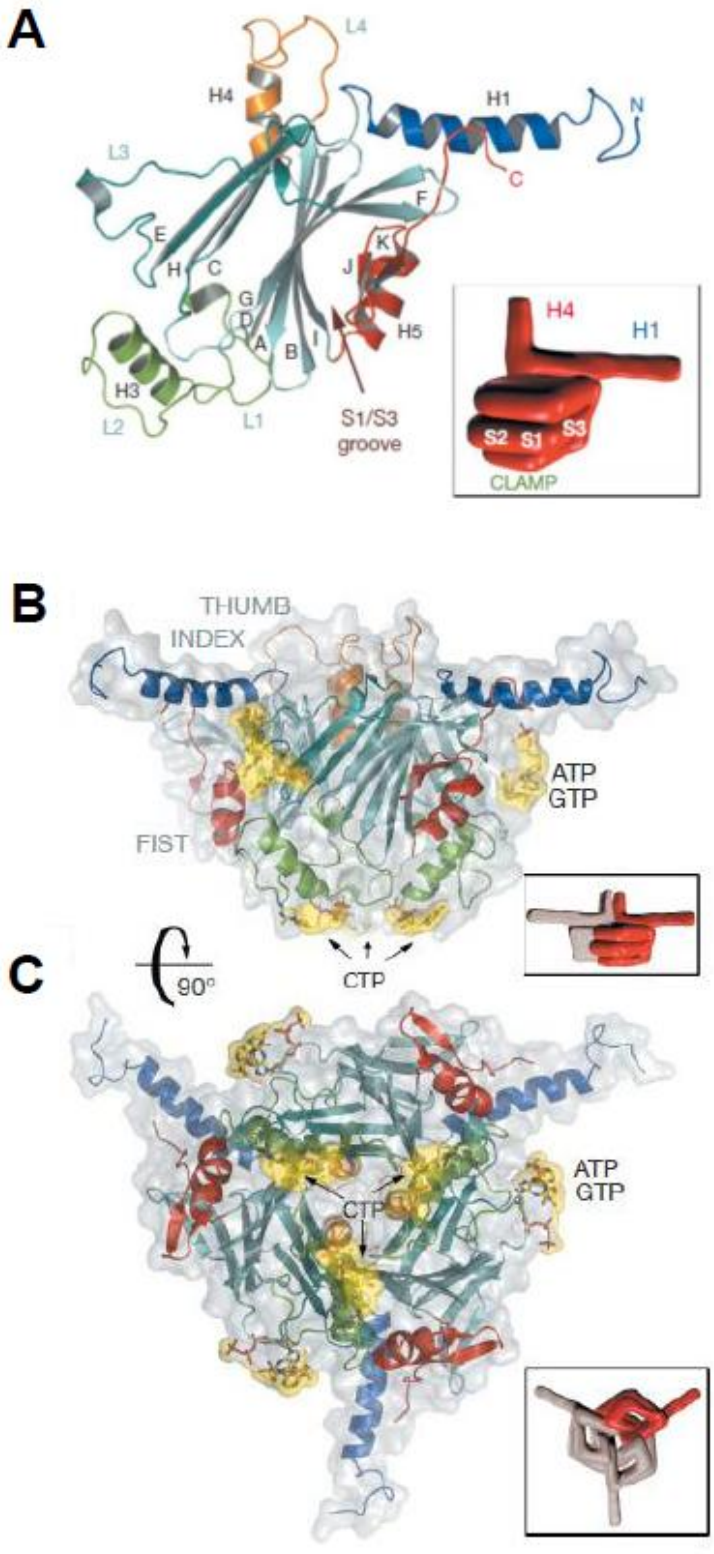

Fig. 3 Structure of BmCPV polyhedrin. (A) Polyhedrin has the shape of a left hand (inset). The finger (H1, blue), thumb (H4, orange), fist (S1–S2, cyan and S3, red) and clamp (H3, green) all contribute to the organization of polyhedra. (B, C) The polyhedrin trimer in two orthogonal views with bound nucleotides shown in a yellow surface. The insets represent trimer models with one of the subunits highlighted in red.

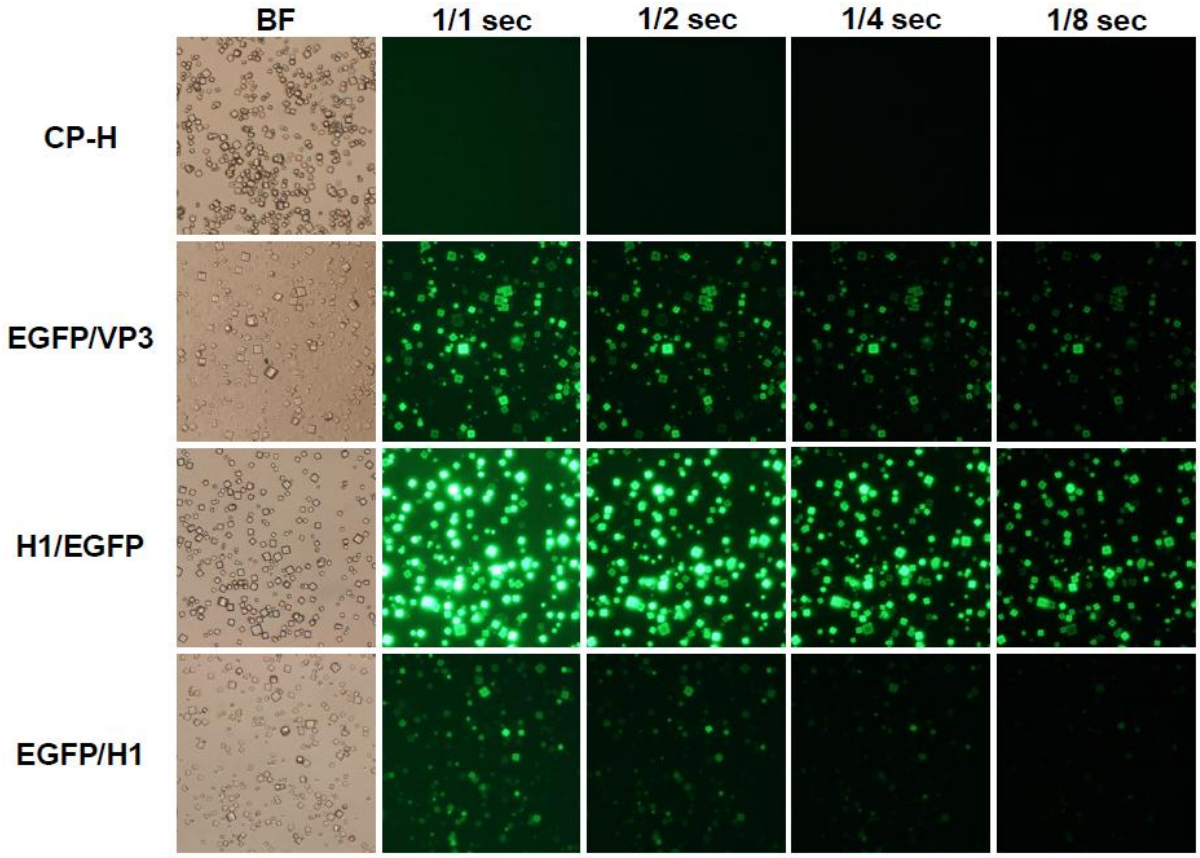

Fig. 4 Comparison of the intensity of green fluorescence from EGFP immobilized into polyhedra. Polyhedra were desiccated on a glass slide at a density of 1 x 10^4 polyhedra per μL. Subsequently, the fluorescence of polyhedra-mounted glass slide were observed by a fluorescent microscope with each exposure times (1/1, 1/2, 1/4 and 1/8 seconds). BF, bright field. Scale bar, 10 μm. (b) Magnified images of polyhedra observed at 1/2 seconds. BF, bright field. Scale bar, 5 μm.

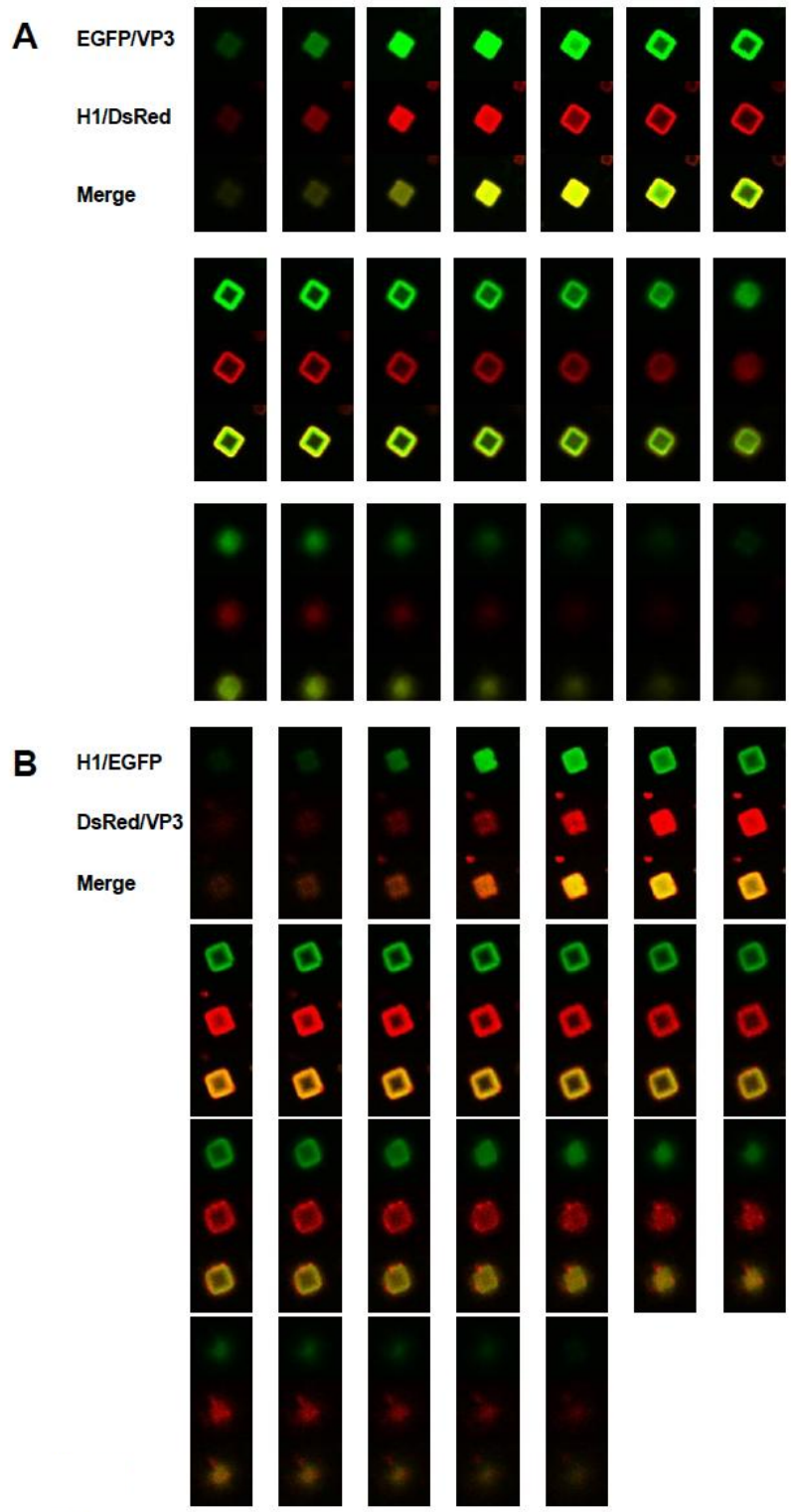

Fig. 5 Analysis of polyhedra containing two recombinant fluorescence proteins by confocal microscopy. (A) Laser-scanning confocal images of one polyhedron containing EGFP/VP3 and H1/DsRed. (B) Laser-scanning confocal images of one polyhedron containing H1/EGFP and DsRed/VP3. Polyhedra were prepared by triple-infection with AcCP-H and two recombinant viruses expressing EGFP and DsRed and optically sectioned using 0.2 μm intervals.

Chapter 2: Control of angiogenesis by VEGF and endostatin-encapsulated protein microcrystals and inhibition of tumor angiogenesis

We have previously reported the encapsulation of fibroblast growth factor-2 (FGF-2) and FGF-7, epidermal growth factor (EGF), leukemia inhibitory factor, and secreted frizzled-related protein 4 into polyhedra (Ijiri et al., 2009; Matsushima et al., 2010; Mori et al., 2007; Nishishita et al., 2011). These cytokines have biological activities as monomers. The vascular endothelial growth factor (VEGF) family plays an integral role in angiogenesis, lymphangiogenesis, and vasculogenesis (Ferrara, 2004; Hoeben et al., 2004). The VEGF family currently comprises seven members (VEGF-A, VEGF-B, VEGF-C, VEGF-D, VEGF-E, VEGF-F, and placental growth factor). All members have a common VEGF homology domain. The core region is composed of a cystine knot motif, with eight invariant cysteine residues involved in inter- and intramolecular disulfide bonds at one end of a conserved central four-stranded β-sheet within each monomer, which dimerize in an antiparallel, side-by-side orientation (Ferrara, 2004; Hoeben et al., 2004; Neufeld et al., 1999; Ortega et al., 1999). VEGF-A is a 34- to 42-kDa, dimeric, disulfide-bound glycoprotein. VEGF-A exists in at least seven homodimeric isoforms where each subunit consists of 121, 145, 148, 165, 183, 189, or 206 amino acids (Ferrara, 2004; Hoeben et al., 2004). Before the encapsulation of VEGF-A into polyhedra, overexpression of protein disulfide bond isomerase (PDI) is required to obtain biologically active VEGF-encapsulated polyhedra.

Endostatin, a 20-kDa C-terminal fragment digested from collagen XVIII, inhibits the proliferation and migration of endothelial cells, and induces apoptosis, leading to repression of growth of a wide variety of tumors with neovascularization (Folkman, 2006; O'Reilly et al., 1997). The apoptotic effect of endostatin is associated with decreased levels of anti-apoptotic molecules (Dixelius et al., 2000). Recently, Zhuo *et al.* reported that endostatin

directly inhibits lymphatic endothelial cells (LEC) and lymphangiogenic vessels via the cell surface receptor nucleolin on LEC which inhibits lymphatic metastasis (Zhuo et al., 2010).

In this study VEGF and endostatin were encapsulated into polyhedra and the effect of both VEGF and endostatin polyhedra on angiogenesis in cell culture and *in vivo* was investigated.

Materials and methods

Medium

Growth medium: EGM-2 (LONZA) containing 2% fetal bovine serum (FBS), EGF, FGF-2, VEGF, R^3-IGF-1, hydrocortisone, ascorbic acid, heparin, GA-100 (gentamicin, amphotericin-B). Assay medium: EGM-2 containing 0.2% FBS, hydrocortisone, ascorbic acid, heparin, GA-1000. Starvation medium: αMEM (WAKO).

Construction of VEGF and endostatin transfer vector

Recombinant VEGF-A baculovirus transfer vectors were generated using GATEWAY® cloning technology (Invitrogen). The VEGF-A gene (189 aa) fused to DNA encoding either VP3 immobilization signal at N-terminal or C-terminal was amplified by polymerase chain reaction (PCR) using primer sets containing *att*B1 and *att*B2 sequences below:

the forward primer is 5’-GGGGACAAGTTTGTACAAAAAAGCAGGCTTAATGGCACCCACGACAGAAGGAGAGC-3’ and reverse primers are 5’-GGGGACCACTTTGTACAAGAAAGCTGGGTATCACCGCCTTGGCTTGTCACATCTGCA-3’ for N-terminal VP3 or 5’-GGGGACCACTTTGTACAAGAAAGCTGGGTACCGCCTTGGCTTGTCACATCTGCA-3’ for C-terminal VP3. The resulting *att*B-flanked PCR products were cloned into a donor vector (pDONR221) to construct entry vectors by BP reactions of GATEWAY® system. The

open reading frame cloned between the *att*L1 and *att*L2 sites in the entry vectors was transferred to destination vectors (pDEST-N-VP3 or pDEST-C-VP3) via LR Clonase™ reactions resulting in production of the transfer vectors encoding VEGF-A fused with VP3 tag (pVP3/VEGF and pVEGF/VP3).

DNA fragment encoding C-terminal region (183 aa) of collagen XVIII was fused with H1 or VP3 immobilization signal and also amplified by PCR using primer sets containing *att*B1 and *att*B2 sequences below:

the forward primer is 5'-GGGGACAAGTTTGTACAAAAAAGCAGGCTTAATGCACAGCCACCGCGACTTCC AGC -3' and reverse primers are 5'-GGGGACCACTTTGTACAAGAAAGCTGGGTACTACTTGGAGGCAGTCATGAAGC TGTT-3' for H1 signal at N-terminal or 5'-GGGGACCACTTTGTACAAGAAAGCTGGGTACTTGGAGGCAGTCATGAAGCTGT T-3' for VP3 signal at C-terminal. The resulting *att*B-flanked PCR products were also cloned into pDONR221 to construct entry vectors. The open reading frame cloned between the *att*L1 and *att*L2 sites in the entry vectors was transferred to destination vectors (pDEST-N-H1 or pDEST-C-VP3) resulting in production of the transfer vectors encoding endostatin fused with H1 or VP3 tags (pH1/Endo and pEndo/VP3).

Production of VEGF and endostatin polyhedra

The transfer vectors were co-transfected into *Spodoptera frugiperda* IPLB-Sf21-AE (Sf21) cells with linearized Baculogold Baculovirus DNA (BD Pharmingen). After incubation for 5 days at 27 ºC, recombinant baculoviruses expressing VEGF-A and endostatin were harvested and stored at 4 ºC. To incorporate VEGF-A into polyhedra (VEGF polyhedra), immobilization of VEGF-A using VP3 tag was accomplished by dual infection of the

recombinant baculoviruses that express the VEGF-A and a recombinant baculovirus AcCP-H expressing BmCPV polyhedrin or AcCP-H/PDI expressing BmCPV polyhedrin and PDI, in which BmCPV polyhedrin and PDI were expressed under the control of the baculovirus polyhedrin promoter and p10 promoter, respectively. Endostatin polyhedra were also made by dual infections with recombinant baculoviruses expressing endostatin with H1 tag (AcH1/Endo) or VP3 tag (AcEndo/VP3) and AcCP-H, resulting in H1/Endo polyhedra and Endo/VP3 polyhedra. To generate empty polyhedra, Sf cells were inoculated with recombinant baculovirus AcCP-H or AcCP-H29/PDI. The infected cells were cultured for 10 days at 27 ºC and then the cells were harvested in a conical tube by centrifugation. The cell pellet was resuspended in phosphate-buffered saline (PBS; pH 7.2) and treated with an ultrasonic homogenizer at 6% power for 30 sec. The cell homogenate was centrifuged at 1500 x g at 4 ºC and the supernatant was removed. These treatments were repeated and the purification was complete. The polyhedron suspension was adjusted to the same density (5 x 10^4 numbers /μL) and stored at 4 ºC in distilled water containing 100 units/mL penicillin and 100 μg/mL streptomycin.

Phosphorylation of p44/p42 mitogen-activated protein kinase (MAP kinase)

Human umbilical vein endothelial cells (HUVECs) were plated into a 6-well plate at a density of 1 x 10^5 cells per well and cultured to confluence in the growth medium. Cells were washed with PBS and then incubated with the starvation medium for 6 hours to synchronize cell cycles. The cultures were then treated with rhVEGF and empty or VEGF polyhedra. HUVECs were washed with PBS twice and dissolved in 100 μL of 1 x SDS sample buffer containing 50 mM Tris-HCl (pH 6.8), 2% SDS, 50 mM dithiothreitol, 0.1% bromophenol blue, and 10% glycerol. Cell lysates were harvested, sonicated, and cleaned by centrifugation. Samples were electrophoresed on 12% SDS-polyacrylamide gels and transferred to

nitrocellulose membranes (Bio-Rad). After preincubation with blocking buffer containing 5% nonfat milk, 0.1% Tween 20, 25mM Tris-HCl (pH 7.6), 150 mM NaCl, the membranes were incubated with either p44/42 MAP Kinase Antibody or Phospho-p44/42 MAP kinase (Thr202/Tyr204) Antibody followed by horseradish peroxidase (HRP)-conjugated anti-rabbit IgG antibody (New England Biolabs). Peroxidase activity was detected and visualized by ECL Western Blotting Detection Reagents (GE Healthcare).

Proliferation assay of HUVECs

The proliferation of HUVECs was measured by Cell Counting Kit-8 using WST-8 (DOJINDO). Cells were seeded into 96-well plates at a density of 3 x 10^3 cells/well. After incubation in the assay medium containing rhVEGF and empty or VEGF polyhedra for 3 days at 37 ºC under 5% CO_2, Cell Counting Kit-8 solution was added to the cultures and incubated for 4 hours at 37 ºC under 5% CO_2, according to the manufacturer's instructions. Absorbance at 450 nm was determined with a microplate reader Model 680 (Bio-Rad).

In vitro scratch assay

We used the *in vitro* scratch assay to assess the activity of VEGF polyhedra and endostatin polyhedra on migration of HUVECs. HUVECs were seeded in 24-well plates (8 x 10^3/well) with the growth medium and cultured to confluence in the growth medium. The cells were scraped away vertically 24 hours later by pipette tip. Each well was washed twice with PBS to remove debris, and then further incubated for 18 hours in serum-free EGM-2 medium with rhVEGF or polyhedra (empty, VEGF, endostatin). Endostatin polyhedra were assayed in the presence of 10 ng/mL rhVEGF. The distances between the 2 edges of the scratch were photographed on each well using an inverted microscope.

Network formation of HUVECs

Subconfluent culture of HUVECs were washed with PBS and suspended in the starvation medium to synchronize cell cycles. After rhVEGF or polyhedra (empty, VEGF, endostatin) were mixed with ECMatrix (CHEMICON) solution, 50 μL of the aliquot were added to each well of the 96-well plate and the plate was incubated for 1 hour at 37 ºC to allow the matrix solution to solidify. To assay endostatin polyhedra, ECMatrix solution containing rhVEGF (10 ng/mL) was used. HUVECs (1 x 10^4/well) were seeded onto presolidified ECMatrix. After incubation for 18 hours at 37ºC under 5% CO_2, 50 μL of Calcein AM (BD Biosciences) solution was added to each well and plates were incubated at 37ºC under 5% CO_2 for 30 minutes. Total tube length of each well was measured using an image analyzer (ESPEC TECHNO CORP).

Tube formation of HUVECs

Normal human dermal fibroblast cells (2 x 10^4/well) were seeded onto a collagen-coated 24-well plate and incubated with 500 μL of Medium 106 supplemented with Low Serum Growth Supplement containing 2% FBS, EGF, FGF-2, hydrocortisone, heparin (Life Technologies) for 24 hours at 37ºC under 5% CO_2. The medium was replaced with the starvation medium and then rhVEGF or polyhedra (empty, VEGF, endostatin) were added to each well followed by incubation for 1 hour at 37ºC under 5% CO_2. Endostatin polyhedra were assayed in the presence of 10 ng/mL rhVEGF. HUVECs (2 x 10^4/well) were seeded into each well and incubated with the assay medium for 11 days at 37ºC under 5% CO_2. The assay medium with or without rhVEGF (10 ng/mL) was used for wells of rhVEGF or polyhedra, respectively, at each 2 days medium change. Cells were washed with PBS and fixed with cold 70% ethanol. After 30 min, ethanol was discarded and cells were incubated with 1% BSA. Fixed cells were reacted with mouse anti-human CD31 antibody and then goat

anti-mouse IgG AP conjugate antibody. Tube formation of HUVEC was detected by addition of substrate BCIP/NBT.

Tumor cell line and cell cultures

The SCC-VII tumors were cutaneous mouse squamous cell carcinomas that spontaneously arose in the C3H/He mouse strain (Chaplin et al., 1987). SCC-VII cells were inoculated subcutaneously into C3H/He mice. We cultured SCC-VII cells in RPMI 1640 medium supplemented with 10% heat-inactivated FCS at 37°C in an incubator with 5% CO_2.

Tumor model and treatment

Our animal studies conformed to the Kanagawa Dental University guidelines for research animal care and were approved by ethical committees of Kanagawa Dental University. Subcutaneous injection of 5 x 10^5 SCC-VII cells in 100 μL of PBS into the backs of C3H/He mice (Japan SLC, Shizuoka, Japan) aged 6 weeks generated back tumors. Tumor volume was estimated using the formula: tumor volume (mm^3) = length (mm) x cross-section $(mm)^2$ x 1/2. Two weeks later, when the tumors had grown to 100-200 mm^3, we randomly divided the mice into 4 treatment groups: 5 x 10^6 H1/Endo polyhedra with 100 μL PBS; 5 x 10^6 Endo/VP3 polyhedra with 100 μL PBS; 5 x 10^6 empty polyhedra with 100 μL PBS; and no treatment as a control. On the 2^{nd} and 4^{th} week after the inoculation of tumor cells, we administered each polyhedron by intratumoral injection. The control group was without treatment. After SCC-VII tumor-cell inoculation, tumor volume was measured at 6 weeks. Each group contained 4 mice.

Immunohistochemical analysis

Implanted-tumor specimens from mice were embedded in OCT compound, quickly frozen

in dry ice, and stored at -80 °C for immunohistochemical staining. To analyze tumor angiogenesis and lymphangiogenesis, we performed double immunofluorescence staining of excised tumors for the vascular marker CD31 and for the lymphatic-specific marker LYVE-1. Frozen sections of 6 μm thickness were stained using a rat anti-mouse CD31 mAb (clone MEC13.3, Pharmingen, CA) for 60 min at RT and then rinsed 3 times. Sections were then stained with anti-rat antibody conjugated with Alexa Fluor 488 (Invitrogen, CA) for 60 min at RT. After staining with CD31, the sections were rinsed 3 times in PBS and incubated a second time with anti-LYVE-1 polyclonal Ab (Abcam, Cambridge, UK) for 60 min at RT and then rinsed 3 times. Sections were then stained with anti-rabbit antibody conjugated with Alexa Fluor 546 (Invitrogen, CA) for 60 min at RT. Cell nuclei were counterstained with DAPI (InnoGenex, CA). Slides were then mounted with a fluorescent mounting medium (DAKO, CA). Images were obtained on a Zeiss microscope and analyzed using AxioImager software (Carl Zeiss, NY). Microvessel density and lymphatic microvessel density in the tumors were determined after immunostaining with antibodies against CD31- and LYVE-1-positive vessels, which were counted microscopically under x100 magnification from 3 areas of the highest vascular density per section.

Results

Proliferation, migration, network and tube formation of HUVECs by VEGF polyhedra

VEGF is secreted as a cysteine-linked dimer and has two binding sites at opposite poles through which it binds VEGF receptors (VEGFRs). VEGFRs are tyrosine kinases found on the surface of endothelial and other cells. VEGF-A tagged with VP3 at N-terminus or C-terminus was incorporated into polyhedra with or without the expression of PDI and biological activities of these polyhedra were studied. To examine activation of the downstream signaling pathway by polyhedra encapsulating VEGF-A, phosphorylation of

p44/p42 MAP kinase was analyzed in HUVECs. Phosphorylated forms of p44 and p42 MAP kinase were detected in HUVECs incubated with rhVEGF as well as VEGF/VP3+PDI polyhedra, in which VEGF-A fused with VP3 at C-terminus and co-expressed with PDI was encapsulated (Fig. 6A). In contrast, phosphorylation was not or was poorly detected in the cells incubated with empty polyhedra, nor was detection observed for other polyhedra in which VEGF-A was encapsulated by VP3 at N-terminus or without PDI expression. The VEGFRs require dimerization to be active. Signaling is initiated when VEGF binds first to one of the receptors, resulting in translocation of the second receptor for dimerization. As it was considered that firstly dimerization of VEGF-A was caused by PDI and then VEGF-A molecules were incorporated into polyhedra, we used these polyhedra as VEGF polyhedra for assay of proliferation, migration, and network and tube formation of HUVECs.

We have previously reported similar results regarding encapsulation of bone morphogenetic protein 2 (BMP-2) into polyhedra (Matsumoto et al., 2012). Native BMP-2 protein consists of two polypeptide chains linked by an S–S bond between Cys78 of each chain. Co-expression of PDI was needed to obtain biologically active BMP-2 polyhedra during encapsulation into polyhedra. BMP-2 expressed in *Escherichia coli* is accumulated in inclusion bodies and the first step of preparation is isolation of inclusion bodies from *E. coli* cells. Secondly, denaturation of inclusion bodies and purification are necessary. Finally, subsequent refolding of BMP-2 is required to attain the biologically active homodimeric form (Sharapova et al., 2010). VEGF is usually expressed in *E. coli* cells and purified by similar steps (Heiring and Muller, 2001; Seyedarabi et al., 2013). Our data show that the isolation and denaturation of inclusion bodies and subsequent refolding into the biologically active homodimeric form are unnecessary when cytokines for encapsulated into polyhedra.

Proliferation of HUVECs in the presence of VEGF polyhedra showed a dose-response curve (Fig. 6B). VEGF activity from 8.75×10^4 numbers of VEGF polyhedra was estimated to be

equivalent to the activity of 1 ng rhVEGF. Endothelial cell migration is a necessary step of angiogenesis. The effect of VEGF polyhedra on HUVECs migration was determined using the scratch assay. As shown in Figure 7, cell migration was stimulated by VEGF polyhedra. The formation of three-dimensional capillary-like structures by HUVECs is well-established in *in vitro* angiogenesis assays. HUVECs were seeded on Matrigel substrate and dispersed evenly throughout the culture. Thereafter, cells spontaneously aligned to form a network of capillary-like structures in the presence of rhVEGF or VEGF polyhedra (Fig. 8A, B). The formation of tube-like structures is an essential step in angiogenesis. Therefore, HUVEC angiogenesis was also observed using the tube formation assay. As shown in Figure 8C, capillary tube structures were formed by rhVEGF or VEGF polyhedra after HUVECs were placed in the wells, indicating that VEGF polyhedra can stimulate angiogenesis.

Antiangiogenic activities of endostatin polyhedra

We studied the antiangiogenic activities of endostatin polyhedra. Endostatin fused with H1 or VP3 tags was incorporated into polyhedra (H1/Endo polyhedra and Endo/VP3 polyhedra, respectively). The antimigratory effect of both endostatin polyhedra was observed by the inhibition of migration of HUVECs (Fig. 7). Addition of endostatin polyhedra to the culture media significantly inhibited the network and tube formation of HUVECs (Fig. 8), indicating that endostatin polyhedra had potent anti-endothelial cell activity.

Inhibition of tumor growth by endostatin polyhedra injections

Approximately 2 weeks later, when the tumors had grown to 100-200 mm^3, the mice were randomly assigned to groups and therapy was initiated. H1/Endo polyhedra, Endo/VP3 polyhedra and empty polyhedra were administrated at 2 and 4 weeks after tumor-cell inoculation. At 6 weeks post-inoculation, the tumor volumes of endostatin polyhedra groups

(H1/Endo polyhedra and Endo/VP3 polyhedra) were lower than those of control or empty polyhedra groups (Fig. 9). We concluded that local therapy with endostatin encapsulated into polyhedra as a carrier efficiently inhibited tumor growth *in vivo*.

To identify the mechanism of tumor growth inhibition, we examined angiogenesis of tumor tissues by immunohistochemical staining. Angiogenesis within the tumor tissues was determined by directly counting the number of $CD31^+$ cells on microvessels. The most highly vascularized areas of each tumor were identified and $CD31^+$ vessels were counted in at least five fields (magnification: x100). Angiogenesis was inhibited in the treatment with H1/Endo polyhedra or Endo/VP3 polyhedra, and there was a significant difference compared to the number of vessels counted for the control and empty polyhedra groups. There was a pronounced inhibition of angiogenesis in tumors treated with the H1/Endo polyhedra or Endo/VP3 polyhedra (Fig. 10B). However for lymphatic vessel assay, no statistically significant differences in lymphatic vessel densities were observed in all experimental groups compared to controls (Fig. 10C). To conclude, endostatin polyhedra were effective in the blood vessel assay but were not effective in the lymphatic vessel assay. Endostatin polyhedra therefore may have anti-angiogenic effect but likely do not have anti-lymphangiogenic effect.

Discussion

Cytokines are not diffusible and bind to the cell surface or surrounding extracellular matrix (ECM) (Ramirez and Rifkin, 2003; Sternlicht and Werb, 2001). FGF-2 binds to heparan sulfate in ECM and ECM-bound FGF-2 is released by exposure to heparin or heparan sulfate (Bashkin et al., 1989). FGF-2 released from ECM is biologically active and stimulates cell proliferation and DNA synthesis in vascular endothelial cells and 3T3 fibroblasts. VEGF and endostatin have heparin-binding domains which are critical in angiogenesis and antiangiogenesis, respectively (Fairbrother et al., 1998; Javaherian et al., 2002; Sasaki et al.,

1999). Release of VEGF and endostatin from ECM and their activation is triggered by the binding of heparin. Such a signaling cue originating from the extracellular microenvironment is also essential for cellular processes including proliferation, differentiation, migration and apoptosis. For *in vivo* study of interactions between cytokines and target cells or tissues, reservoirs or slow-release agents are necessary for sustained release of active cytokines. If the cytokines are unstable molecules, such a reservoir might be more important for *in vivo* study.

Dr. Folkman observed that endostatin has potent antiangiogenesis activity and endostatin was effective in inhibiting tumor growth in several preclinical studies, however the response in clinical trials was less impressive. It was difficult for other laboratories to reproduce these experiments. There are some practical problems in expression, refolding, bioavailability, short half-life, purification and stock of endostatin due to its instability (Fu et al., 2009). There are various methods by which to transfect endostatin cDNA into cells. One way is to use a viral vector to incorporate the gene or gene fragment into the cells (Noro et al., 2004; Sun et al., 2005). While this method allows effective and reliable supply of endostatin in the cell, there is an unavoidable risk that the virus may cause harm to the host.

To mitigate these problems, we have genetically modified endostatin to improve its biological activity. The modified cypovirus polyhedra can function as nano- or micro-containers stabilizing incorporated proteins in a functional form (Mori, 2010). One application is as a mimic of ECM whereby cytokines including growth factors can be expressed in the polyhedra to mimic their natural structural scaffolds such as collagen, fibronectin and heparan sulfate. In the ECM, enhanced stability and activity of the embedded cytokines results in cell proliferation and differentiation regulated in time and space (Ramirez and Rifkin, 2003; Sternlicht and Werb, 2001). Such perspectives can drive active research on the applications of polyhedra in stem cell research, tissue engineering and regenerative medicine. Another application is a novel tool for “proof of concept”. Unstable cytokine

molecules are rapidly degraded and the biological activities are lost. However, purification of cytokines becomes unnecessary when encapsulating within polyhedra. We would like to propose the use of polyhedra for elucidation or identification of unknown functions of cytokines.

Tumor growth and metastatic dissemination depend on the formation of new tumor microvessels. The process of tumor angiogenesis is a balance between proangiogenic and antiangiogenic factors. The use of antiangiogenic agents to restore this balance represents a useful approach in cancer treatment. Inhibition of tumor angiogenesis by antiangiogenic agents for anticancer therapy is widely accepted.

Generally, the lymphatic system plays important roles in maintaining fluid balance in inflammation and cancer (Cao, 2005; Swartz, 2001). In cancer, lymphangiogenesis, the sprouting of new lymphatic vessels from the preexisting lymphatic system, may provide a way to facilitate the dissemination of tumor cells to sentinel lymph nodes and other distant organs (Cao, 2005; Gao et al., 2009). Recently, several researchers reported that endostatin inhibits lymph node metastasis via down-regulation of VEGF-C, either by tumor cells or by mast cells in the tumor micro-environment (Brideau et al., 2007; Fukumoto et al., 2005). Interestingly, endostatin directly acts on lymphangiogenic endothelial cells via cell surface receptor nucleolin on LECs and inhibits tumor lymphangiogenesis (Zhuo et al., 2010). Here, we did not detect the effects of endostatin on tumor lymphangiogenesis and lymph node metastasis. These discrepancies may be due to the use of different tumor models. SCC-VII tumors are cutaneous mouse squamous cell carcinomas that spontaneously arise in the C3H/He mouse strain and do not metastasize (Matsumoto et al., 2001).

Antiangiogenic cancer therapy with antiangiogenic agents requires the peptide to be administered regularly or daily over a prolonged period, implying that large quantities of the therapeutic agent are needed. These functional antiangiogenic proteins are expensive to

produce, and frequently there are technical problems related to physical properties and purity. Moreover, some therapeutic agents that could otherwise provide effective antiangiogenic cancer therapy have biological half-lives too short to sustain tumor regression. All of the above factors are obstacles for effective therapies using exogenously injected antiangiogenic agents to inhibit tumor angiogenesis. Polyhedral microcrystals represent an attractive and promising alternative method to deliver antiangiogenic agents. We reported that polyhedron microcrystals can remain in the connective tissue over five weeks after implantation (Matsumoto et al., 2012). Consequently, therapy using polyhedral microcrystals has the potential to produce the antiangiogenic agent in high concentrations in a tumor area over a sustained period, thereby avoiding the problems encountered with long-term administration of recombinant proteins.

Conclusion

VEGF fused with VP3 tag at the C-terminus was co-expressed with PDI and encapsulated into insect virus-derived protein microcrystals, polyhedra. The polyhedra stimulated phosphorylation of P44/P42 MAP kinase of HUVECs. VEGF polyhedral stimulated angiogenesis as revealed by assays of proliferation, migration, and network and tube formation of HUVECs. Endostatin fused with H1 tag at N-terminus or VP3 at C-terminus was encapsulated into polyhedra. Endostatin polyhedral showed potent anti-endothelial activity as they inhibited the migration and network and tube formation of HUVECs. Our data suggest that endostatin polyhedra may have promise for the treatment of experimental squamous cell carcinoma by inhibiting tumors angiogenesis. Further studies are needed to establish optimal protocols including dosage and scheduling for antiangiogenic therapy using endostatin polyhedra.

References

Bashkin, P., Doctrow, S., Klagsbrun, M., Svahn, C.M., Folkman, J., and Vlodavsky, I. (1989). Basic fibroblast growth factor binds to subendothelial extracellular matrix and is released by heparitinase and heparin-like molecules. Biochemistry *28*, 1737-1743.

Brideau, G., Makinen, M.J., Elamaa, H., Tu, H., Nilsson, G., Alitalo, K., Pihlajaniemi, T., and Heljasvaara, R. (2007). Endostatin overexpression inhibits lymphangiogenesis and lymph node metastasis in mice. Cancer Res *67*, 11528-11535.

Cao, Y. (2005). Opinion: emerging mechanisms of tumour lymphangiogenesis and lymphatic metastasis. Nat Rev Cancer *5*, 735-743.

Chaplin, D.J., Olive, P.L., and Durand, R.E. (1987). Intermittent blood flow in a murine tumor: radiobiological effects. Cancer Res *47*, 597-601.

Dixelius, J., Larsson, H., Sasaki, T., Holmqvist, K., Lu, L., Engstrom, A., Timpl, R., Welsh, M., and Claesson-Welsh, L. (2000). Endostatin-induced tyrosine kinase signaling through the Shb adaptor protein regulates endothelial cell apoptosis. Blood *95*, 3403-3411.

Fairbrother, W.J., Champe, M.A., Christinger, H.W., Keyt, B.A., and Starovasnik, M.A. (1998). Solution structure of the heparin-binding domain of vascular endothelial growth factor. Structure *6*, 637-648.

Ferrara, N. (2004). Vascular endothelial growth factor: basic science and clinical progress. Endocr Rev *25*, 581-611.

Folkman, J. (2006). Antiangiogenesis in cancer therapy--endostatin and its mechanisms of action. Exp Cell Res *312*, 594-607.

Fu, Y., Tang, H., Huang, Y., Song, N., and Luo, Y. (2009). Unraveling the mysteries of endostatin. IUBMB Life *61*, 613-626.

Fukumoto, S., Morifuji, M., Katakura, Y., Ohishi, M., and Nakamura, S. (2005). Endostatin inhibits lymph node metastasis by a down-regulation of the vascular endothelial growth

factor C expression in tumor cells. Clin Exp Metastasis *22*, 31-38.

Gao, P., Zhou, G.Y., Zhang, Q.H., Su, Z.X., Zhang, T.G., Xiang, L., Wang, Y., Zhang, S.L., and Mu, K. (2009). Lymphangiogenesis in gastric carcinoma correlates with prognosis. J Pathol *218*, 192-200.

Heiring, C., and Muller, Y.A. (2001). Folding screening assayed by proteolysis: application to various cystine deletion mutants of vascular endothelial growth factor. Protein Eng *14*, 183-188.

Hoeben, A., Landuyt, B., Highley, M.S., Wildiers, H., Van Oosterom, A.T., and De Bruijn, E.A. (2004). Vascular endothelial growth factor and angiogenesis. Pharmacol Rev *56*, 549-580.

Ijiri, H., Coulibaly, F., Nishimura, G., Nakai, D., Chiu, E., Takenaka, C., Ikeda, K., Nakazawa, H., Hamada, N., Kotani, E., *et al.* (2009). Structure-based targeting of bioactive proteins into cypovirus polyhedra and application to immobilized cytokines for mammalian cell culture. Biomaterials *30*, 4297-4308.

Javaherian, K., Park, S.Y., Pickl, W.F., LaMontagne, K.R., Sjin, R.T., Gillies, S., and Lo, K.M. (2002). Laminin modulates morphogenic properties of the collagen XVIII endostatin domain. J Biol Chem *277*, 45211-45218.

Matsumoto, G., Ohmi, Y., and Shindo, J. (2001). Angiostatin gene therapy inhibits the growth of murine squamous cell carcinoma in vivo. Oral Oncol *37*, 369-378.

Matsumoto, G., Ueda, T., Shimoyama, J., Ijiri, H., Omi, Y., Yube, H., Sugita, Y., Kubo, K., Maeda, H., Kinoshita, Y., *et al.* (2012). Bone regeneration by polyhedral microcrystals from silkworm virus. Sci Rep *2*, 935.

Matsushima, K., Suyama, T., Takenaka, C., Nishishita, N., Ikeda, K., Ikada, Y., Sawa, Y., Jakt, L.M., Mori, H., and Kawamata, S. (2010). Secreted frizzled related protein 4 reduces fibrosis scar size and ameliorates cardiac function after ischemic injury. Tissue Eng Part A *16*,

3329-3341.

Mori, H., Metcalf, P. (2010). Cypoviruses. In Insect Virology, S. Asgari, Johnson, K. N., ed. (Caister Academic Press), pp. 307-324.

Mori, H., Shukunami, C., Furuyama, A., Notsu, H., Nishizaki, Y., and Hiraki, Y. (2007). Immobilization of bioactive fibroblast growth factor-2 into cubic proteinous microcrystals (Bombyx mori cypovirus polyhedra) that are insoluble in a physiological cellular environment. J Biol Chem *282*, 17289-17296.

Neufeld, G., Cohen, T., Gengrinovitch, S., and Poltorak, Z. (1999). Vascular endothelial growth factor (VEGF) and its receptors. FASEB J *13*, 9-22.

Nishishita, N., Ijiri, H., Takenaka, C., Kobayashi, K., Goto, K., Kotani, E., Itoh, T., Mori, H., and Kawamata, S. (2011). The use of leukemia inhibitory factor immobilized on virus-derived polyhedra to support the proliferation of mouse embryonic and induced pluripotent stem cells. Biomaterials *32*, 3555-3563.

Noro, T., Miyake, K., Suzuki-Miyake, N., Igarashi, T., Uchida, E., Misawa, T., Yamazaki, Y., and Shimada, T. (2004). Adeno-associated viral vector-mediated expression of endostatin inhibits tumor growth and metastasis in an orthotropic pancreatic cancer model in hamsters. Cancer Res *64*, 7486-7490.

O'Reilly, M.S., Boehm, T., Shing, Y., Fukai, N., Vasios, G., Lane, W.S., Flynn, E., Birkhead, J.R., Olsen, B.R., and Folkman, J. (1997). Endostatin: an endogenous inhibitor of angiogenesis and tumor growth. Cell *88*, 277-285.

Ortega, N., Hutchings, H., and Plouet, J. (1999). Signal relays in the VEGF system. Front Biosci *4*, D141-152.

Ramirez, F., and Rifkin, D.B. (2003). Cell signaling events: a view from the matrix. Matrix Biol *22*, 101-107.

Sasaki, T., Larsson, H., Kreuger, J., Salmivirta, M., Claesson-Welsh, L., Lindahl, U.,

Hohenester, E., and Timpl, R. (1999). Structural basis and potential role of heparin/heparan sulfate binding to the angiogenesis inhibitor endostatin. EMBO J *18*, 6240-6248.

Seyedarabi, A., Cheng, L., Zachary, I., and Djordjevic, S. (2013). Production of soluble human vascular endothelial growth factor VEGF-A165-heparin binding domain in Escherichia coli. PLoS One *8*, e55690.

Sharapova, N.E., Kotnova, A.P., Galushkina, Z.M., Lavrova, N.V., Poletaeva, N.N., Tukhvatulin, A.E., Semikhin, A.S., Gromov, A.V., Soboleva, L.A., Ershova, A.S., *et al.* (2010). [Production of the recombinant human bone morphogenetic protein-2 in Escherichia coli and testing of its biological activity in vitro and in vivo]. Mol Biol (Mosk) *44*, 1036-1044.

Sternlicht, M.D., and Werb, Z. (2001). How matrix metalloproteinases regulate cell behavior. Annu Rev Cell Dev Biol *17*, 463-516.

Sun, X., Krissansen, G.W., Fung, P.W., Xu, S., Shi, J., Man, K., Fan, S.T., and Xu, R. (2005). Anti-angiogenic therapy subsequent to adeno-associated-virus-mediated immunotherapy eradicates lymphomas that disseminate to the liver. Int J Cancer *113*, 670-677.

Swartz, M.A. (2001). The physiology of the lymphatic system. Adv Drug Deliv Rev *50*, 3-20.

Zhuo, W., Luo, C., Wang, X., Song, X., Fu, Y., and Luo, Y. (2010). Endostatin inhibits tumour lymphangiogenesis and lymphatic metastasis via cell surface nucleolin on lymphangiogenic endothelial cells. J Pathol *222*, 249-260.

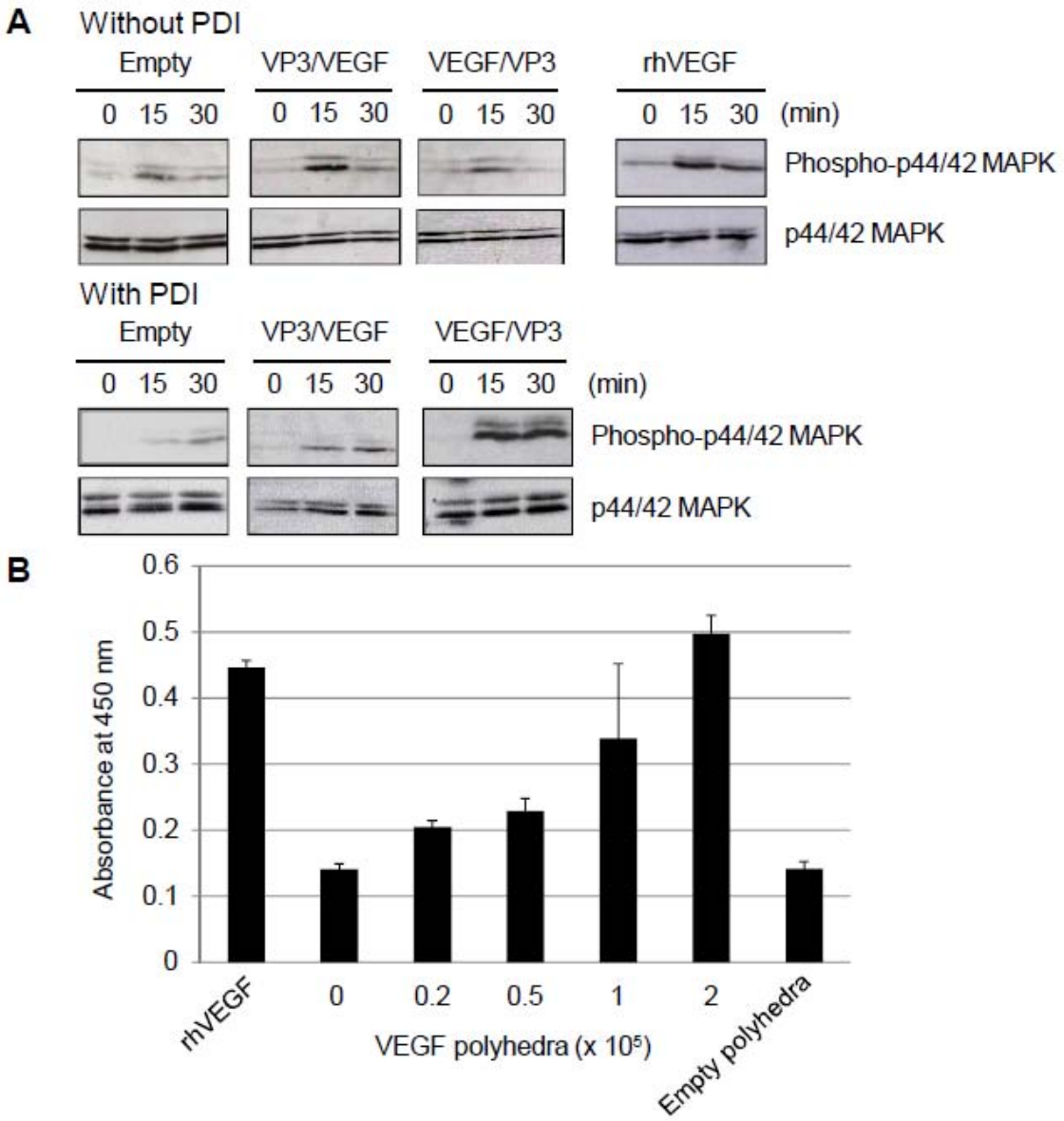

Fig. 6 Phosphorylation of p44/p42 MAP kinase and proliferation of HUVECs by polyhedra encapsulating VEGF-A. (A) HUVECs were plated into a 6-well plate at a density of 1 x 10^5 cells per well and cultured to confluence in the growth medium. Cells were starved in the starvation medium for 6 hours and then incubated with rhVEGF (5 ng/mL) and empty or VEGF polyhedra (2.5 x 10^5 numbers/mL) for 30 min. VP3/VEGF and VEGF/VP3 show VEGF polyhedra in which VEGF was encapsulated into polyhedra by VP3 tag at N- or C-terminus with or without PDI, respectively. Empty is CP-H polyhedra. The phosphorylated p44 (phospho-p44) and p42 (phospho-p42) MAP kinase were immunoblotted with Phospho-p44/p42 MAP Kinase Antibody and total amounts of p44/p42 were detected by p44/p42 MAP Kinase Antibody. (B) HUVECs were plated into a 96-well plate at a density of 3 x 10^3 cells per well and starved in the starvation medium for 6 hours. Each number (0.2, 0.5, 1, 2 x 10^5) of VEGF polyhedra, 2 x 10^5 numbers of empty polyhedra and 2 ng of rhVEGF in 200 μL of the assay medium were added into wells. After 3 days, the proliferation of HUVECs was measured by Cell Counting Kit-8. The graph shows mean +/- S.E.

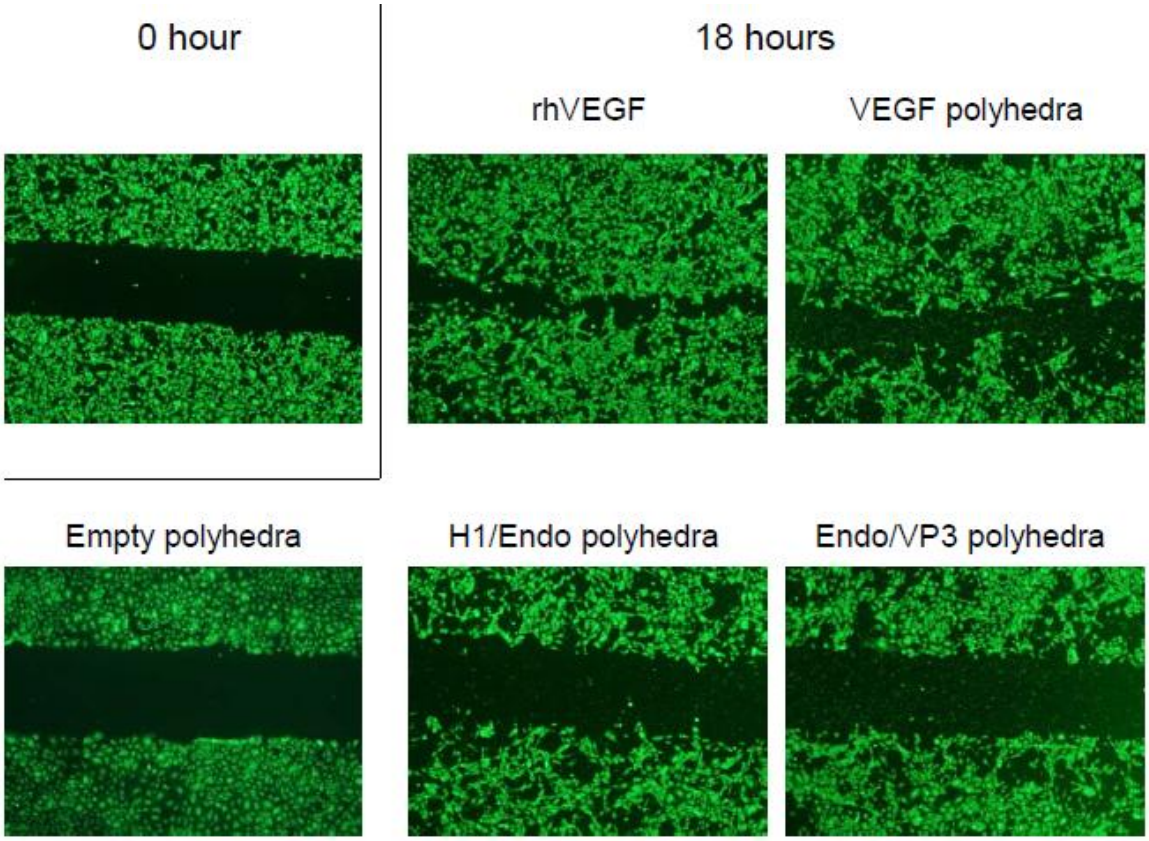

Fig. 7 Stimulation and inhibition of migration of HUVECs by VEGF and endostatin polyhedra. HUVECs were plated into a 24-well plate at a density of 8 x 10^3 cells per well and cultured to confluence in the growth medium. The cells were scraped away vertically by pipette tip and then incubated for 18 hours in 500 μL of serum-free EGM-2 medium with 5 ng of rhVEGF or 4 x 10^5 numbers of empty and VEGF polyhedra. For endostatin polyhedra (H1/Endo polyhedra and Endo/VP3), 4 x10^5 numbers of polyhedra were added to 500 μL of serum-free EGM-2 medium containing rhVEGF (10 ng/mL).

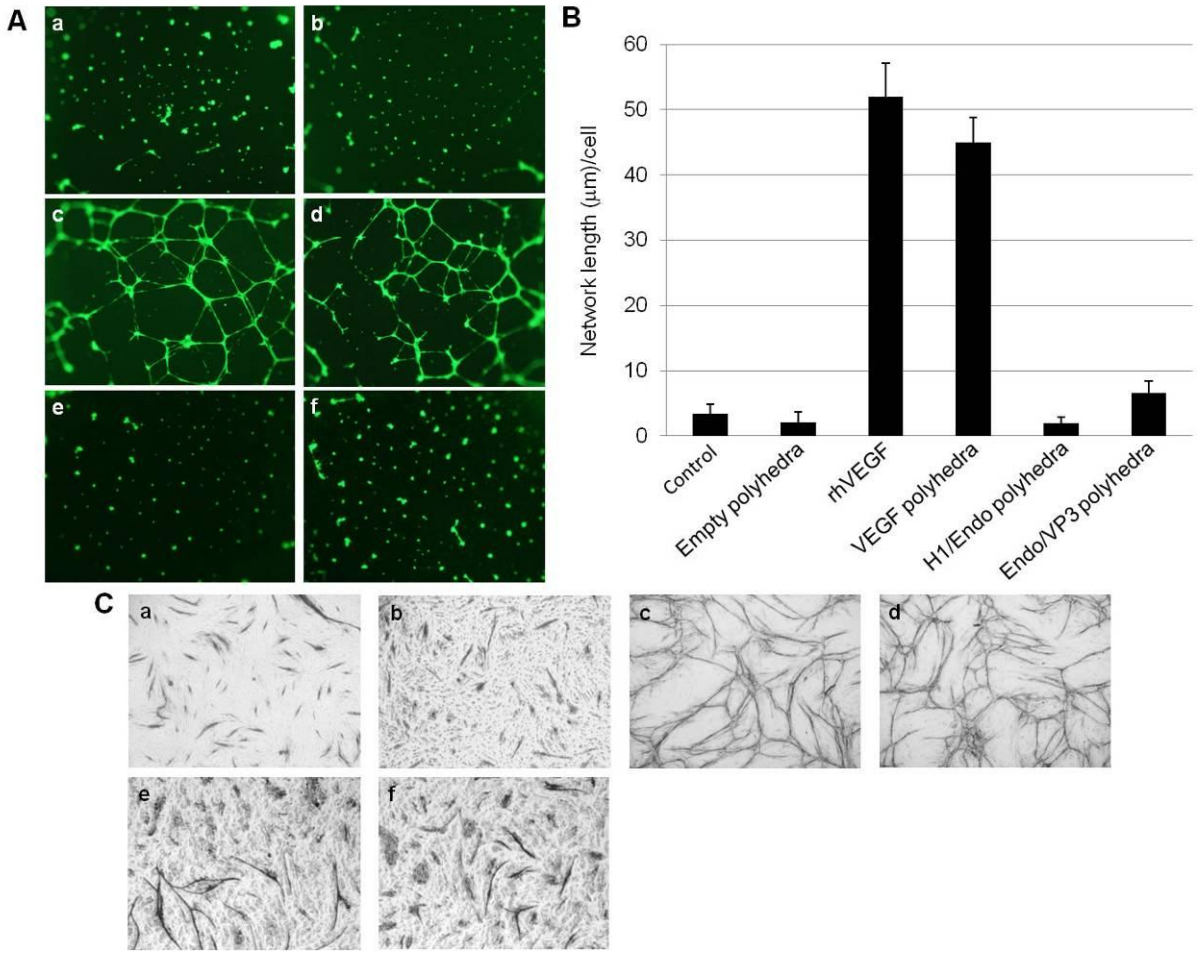

Fig. 8 Stimulation and inhibition of network and tube formation of HUVECs by VEGF and endostatin polyhedra. (A) Subconfluent culture of HUVECs was suspended in the starvation medium to synchronize cell cycles. After 2 ng of rhVEGF or 1.6 x 10^5 numbers of empty and VEGF polyhedra were mixed with ECMatrix solution, aliquots were added to each well of the 96-well plate and incubated at 37 ºC to solidify the matrix solution. For endostatin polyhedra (H1/Endo and Endo/VP3), 1.6 x 10^5 numbers of polyhedra were added to ECMatrix solution containing rhVEGF (10 ng/mL). HUVECs (1 x 10^4/well) were seeded onto presolidified ECMatrix in each well. Calcein AM solution was added to each well. a, control; b, empty polyhedra; c, rhVEGF; d, VEGF polyhedra; e, H1/Endo polyhedra; f, Endo/VP3 polyhedra. (B) Network formation was photographed using an inverted microscope and tube length of each cell was measured using an image analyzer (ESPEC TECHNO CORP). The graph shows mean +/- S.E. (C) Normal human dermal fibroblast cells were plated into a collagen-coated 24-well plate at a density of 2 x 10^4 cells per well and incubated with 500 μL of Medium 106 supplemented with Low Serum Growth Supplement. The medium was replaced with 500 μL of the starvation medium and then 5 ng of rhVEGF or 4 x 10^5 numbers of empty and VEGF polyhedra were added to each well. For endostatin polyhedra (H1/Endo and Endo/VP3), 4 x 10^5 numbers of polyhedra were added to 500 μL of the starvation medium containing rhVEGF (10 ng/mL). HUVECs (2 x 10^4/well) were seeded into each well and incubated with the assay medium for 11 days at 37ºC. The assay medium with or without rhVEGF (10 ng/mL)

was used for wells of rhVEGF and polyhedra, respectively, at each 2 days medium change. To detect tube formation of HUVECs, mouse anti-human CD31 antibody was employed followed by goat anti-mouse IgG AP conjugate antibody. Tubes were observed by addition of substrate BCIP/NBT. a, control; b, empty polyhedra; c, rhVEGF; d, VEGF polyhedra; e, H1/Endo polyhedra; f, Endo/VP3 polyhedra.

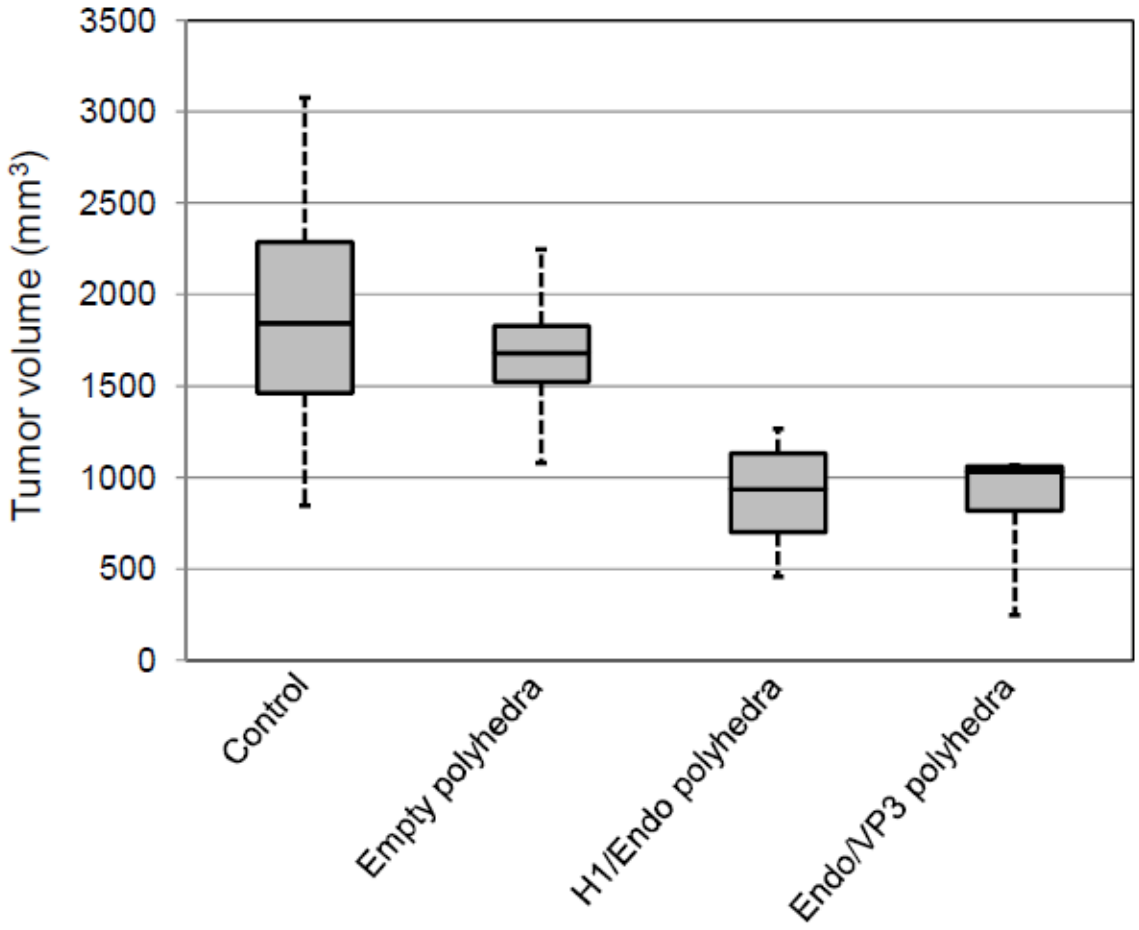

Fig. 9 Inhibition of growth of subcutaneous SCC-VII tumors by intratumoral injection of endostatin polyhedra. Four treatment groups were established: H1/Endo polyhedra, Endo/VP3 polyhedra, empty polyhedra and no treatment as control. Each polyhedron was administrated at 2 and 4 weeks after SCC-VII tumor-cell inoculation and tumor volume was measured at 6 weeks after the tumor-cell inoculation. The first quartile and third quartile were indicated by horizontal bars at the bottom and top of the box, respectively. Median is indicated as the center line inside the box. Outliers are indicated by dots.

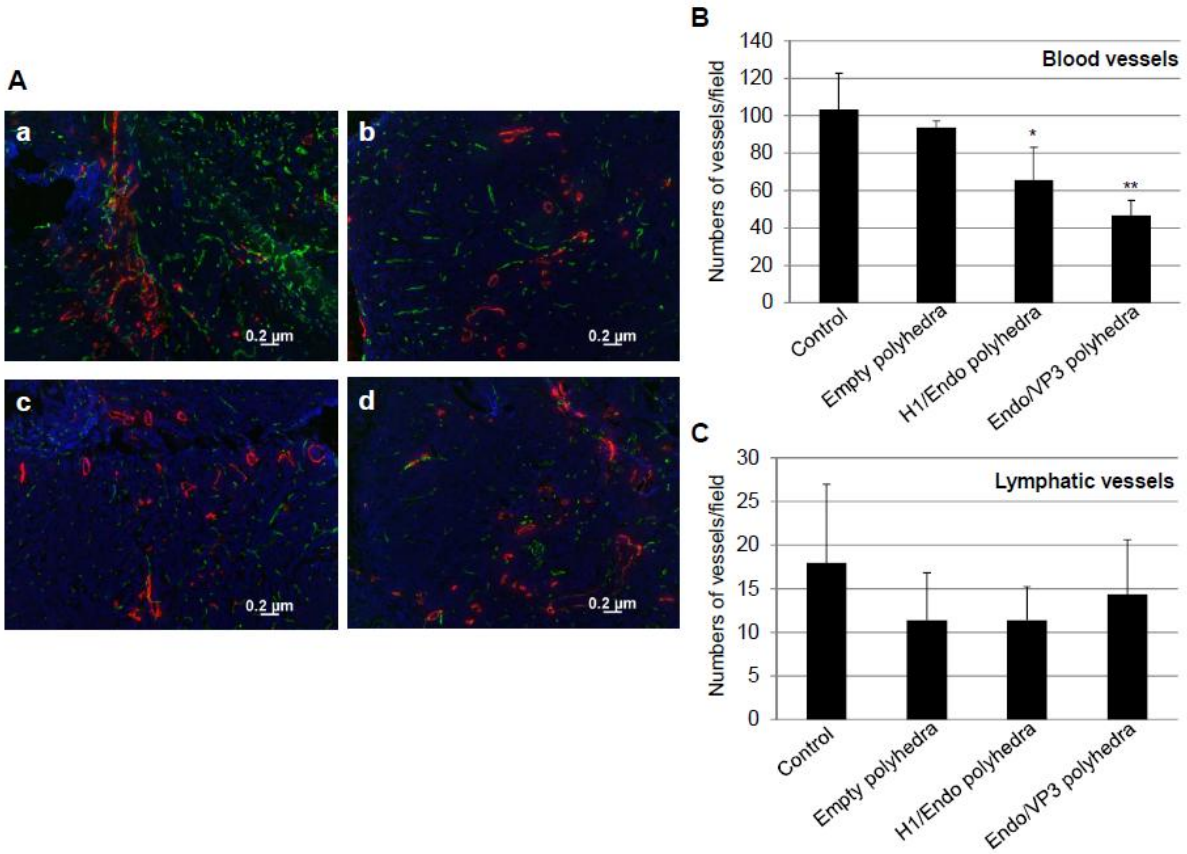

Fig. 10 Endostatin polyhedra inhibit angiogenesis but not lymphangiogenesis in SCC-VII tumors. (A) Representative double immunofluorescent staining image for CD31, the marker of vascular endothelial cells (green), and LYVE-1, the marker of lymphatic endothelial cells (red). a, control; b, empty polyhedra; c, H1/Endo polyhedra; d, Endo/VP3 polyhedra. (B) CD31-positive endothelial cells were randomly counted at 100-power magnification from five different fields. CD31-positive vessels in treated tumors treated with endostatin polyhedra (H1/Endo polyhedra and Endo/VP3 polyhedra) were markedly lower than for control and empty polyhedra groups (*P< 0.05, **P< 0.01). Vessel numbers were compared using Student's t test. The graph shows mean +/- S.E. (C) Quantification of LYVE-1-positive lymphatic vessels in the tumor tissues. There was no significant difference between the control, empty polyhedron, and endostatin polyhedra groups (H1/Endo polyhedra and Endo/VP3 polyhedra). Vessel numbers were compared using Student's t test. The graph shows mean +/- S.E.

Chapter 3: Protein microcrystals encapsulating bone morphogenetic protein 2 support long-term osteogenicity and facilitate healing of critical-sized bone defects by a slow-releasing effect

Tumor resection, delayed bone fracture, congenital abnormalities, and osteonecrosis can all produce defects in bone that require clinical attention and treatment. Until recently, autografting has been the gold standard for clinically managing bone defects. However, bone for an autogenous bone graft must be harvested from a donor site, which introduces the risk of infection and hemorrhage and has other significant disadvantages. Bone-tissue engineering has the potential to identify bone-regeneration techniques that overcome these disadvantages. In complex clinical conditions associated with bone repair and regeneration, more than one healing factor is needed. When the healing conditions are expected to be marginal, more factors such as an adequate osteosynthetic device, growth factors, and/or progenitor cells must be supplied. The basic strategy incorporates one or more of the elements that are needed to regenerate bone tissue into the target site such as scaffolding, growth factors, and osteogenic progenitor cells, which then induce bone formation and guide the tissue-repair function of the living body by encouraging osteogenic cells to migrate, proliferate, and differentiate (Petite et al., 2000).

Bone morphogenetic protein (BMP) is a member of the transforming growth factor-β (TGF-β) superfamily and is a disulfide-linked homodimer that induces bone and cartilage formation. BMP-2 has been shown to induce new bone formation in animal models and is now well recognized as one of the key osteogenic factors in the field of bone-tissue engineering (Reddi, 1994, 1997; Schmitt et al., 1999). BMP-2 induces bone regeneration in fracture healing by activating a set of cellular events including chemotaxis of uncommitted mesenchymal cells and differentiation of these cells into osteoblasts (Fiedler et al., 2002; Mont et al., 2004). BMP-2 has been approved for limited clinical use in the form of recombinant human BMP-2 (rhBMP-2) (Bishop and Einhorn, 2007). However, therapeutic use of rhBMP-2 has been hampered by the

lack of an efficacious way to deliver this protein to the site of the regenerating bone. We have thus sought to identify an appropriate carrier to facilitate retention of rhBMP-2 at the healing site in order to reduce the required dose. A good way to deliver rhBMP-2 to the healing site is via a carrier material. The preferred carrier is a scaffold that is biocompatible, biodegradable, non-toxic, and is immunologically inert in order to avoid tissue rejection. However, the most important requirement for a carrier is that it controls the release of the growth factor it delivers. The carrier materials for BMP-2 that are currently clinically available are not ideal because large amounts of BMP-2 are required to achieve the desired osteogenic results (Jeppsson et al., 1999; Zabka et al., 2001). Despite the ready availability of rhBMP-2 for clinical use, the dilemma facing clinicians and the biotechnology industry is how to achieve an optimal delivery system that can decrease the dose of BMP-2 applied, maintain a more sustained release pattern, and effectively promote osteoconduction (Meikle, 2007). Many growth factors are physiologically stored in the extracellular matrix, some of which are bound to heparan sulfate chains of proteoglycans (Kanematsu et al., 2004; Schonherr and Hausser, 2000). They are released when enzymes secreted by invading or growing cells digest their anchors (Lutolf et al., 2003; Rizzi et al., 2006). Carriers act as delivery systems for rhBMP-2 by retaining it at the site of the bone defect for a prolonged period of time and by providing initial support for the attachment of cells and formation of regenerated tissue. In addition, carriers should have the ability to protect rhBMP-2 from degradation for a sufficient period to induce the desired amount of bone mass at the treatment site. Incorporated rhBMP-2 should be continuously released and controlled because of its very short half-life *in vivo*. Consequently, numerous natural or synthetic biomaterials have been developed to deliver rhBMP-2 (Boerckel et al., 2011; Jeon et al., 2007; Saito et al., 2001).

Materials and methods

Materials

BaculoGold™-linearized baculovirus DNA was purchased from BD Biosciences Pharmingen.

Fetal bovine serum was purchased from Biological Industries for mammalian cell culture and BioWest for insect cell culture. Dulbecco's modified Eagle's/Ham's F12 medium (1:1), insulin and alcian blue solution were purchased from Wako pure chemical industries. Transferrin was from Roche Applied Sciences. Sodium Selinite and Alizarin red were from Sigma-Aldrich. Recombinant human BMP-2 (rhBMP-2) and anti-rhBMP-2 antibody were purchased from R&D systems. All other chemicals and reagents were purchased from Nacalai Tesque.

Construction of BMP-2 polyhedra

The cDNA encoding the BMP-2 ORF was purchased from Toyobo in an entry vector and subcloned into each destination vector (pDEST/VP3-S(N), pDEST/VP3-S(C), pDEST/VP3-L and pDEST/H1) using LR clonase according to the manufacturer's directions. Four types of transfer vector were produced: pTransVP3-S(N)/full-length BMP-2, pTransVP3-S(C)/full-length BMP-2, pTransVP3-L/full-length BMP-2 and pTransH1/full-length BMP-2.

For subcloning of the BMP-2 gene encoding the pro-form (proBMP-2, 24-396 amino acids) or the mature form (mBMP-2, 293-396 amino acids), DNA fragments were amplified by PCR using different primer combinations: forward primers were 5'-GGGGACAAGTTTGTACAAAAAAGCAGGCTCCATGCAAGCCAAACACAAACAG CGGA-3',
5'-GGGGACAAGTTTGTACAAAAAAGCAGGCTCCCAAGCCAAACACAAACAGCGG AAAC-3' and
5'-GGGGACAAGTTTGTACAAAAAAGCAGGCTCCCTCGTTCCGGAGCTGGGC-3', and reverse primers were
5'-GGGGACCACTTTGTACAAGAAAGCTGGGTAGCGACACCCACAACCCTCCACA ACC-3' and
5'-GGGGACCACTTTGTACAAGAAAGCTGGGTACTAGCGACACCCACAACCCTCC

ACAACC-3'. attB-flanked PCR products were then inserted into the donor vector (pDONR221) using a BP clonase reaction. Each BMP-2 gene, cloned between attL1 and attL2 sites in the entry vector, were transferred to destination vectors via LR clonase reactions resulting in production of the transfer vectors encoding the mature or the pro-form of BMP-2 fused with VP3 or H1 tags (pTransVP3-S(N)/pro-form BMP-2, pTransVP3-L/pro-form BMP-2, pTransH1/pro-form BMP-2, pTransVP3-S(C)/mature BMP-2, pTransVP3-L/mature BMP and pTransH1/mature BMP-2). These transfer vectors were co-transfected into Sf21 insect cells with BaculoGold^{TM} baculovirus linearized DNA. After incubation for 5 days at 27 ºC, recombinant baculoviruses expressing the full-length, pro-form, and mature forms of BMP-2 with VP3 or H1 tags were harvested and stored at 4 ºC.

Purification of polyhedra immobilized with BMP-2 proteins

To generate empty polyhedra, *Spodoptera frugiperda* IPLB-SF21-AE cells (Sf cells) were inoculated with recombinant baculovirus AcCP-H29/PDI expressing BmCPV polyhedrin and protein disulfide bond isomerase (PDI), in which BmCPV polyhedrin and PDI were expressed under the control of the baculovirus polyhedrin promoter and p10 promoter, respectively. For production of BMP-2 polyhedra, Sf cells were co-infected with AcCP-H29/PDI and another recombinant baculovirus expressing recombinant BMP-2 fused with the VP3 or H1 tags. Sf cells were also infected with AcCP-H29/PDI to make empty BmCPV polyhedra (CP-H). The infected cells were cultured for 10 days at 27 ºC and then the cells were harvested in a conical tube by centrifugation. The cell pellet was resuspended in phosphate-buffered saline (PBS; pH 7.2) and treated with an ultrasonic homogenizer at 6% power for 30 sec. The cell homogenate was centrifuged at 1500 x g at 4 ºC and the supernatant was removed. These treatments were repeated and the purification was complete. The polyhedron suspension was adjusted to the same density (5 x 10^4 cubes per microliter volume) and stored at 4 ºC in distilled water containing 100

units/mL penicillin and 100 μg/mL streptomycin.

Cell culture

ATDC5 cells were maintained in culture medium containing DME/Ham's F12 (1:1) medium with 10 μg/mL insulin, 10 μg/mL transferrin, 3.2 x 10^{-8} M sodium selenite, 5% fetal bovine serum, 100 units/mL penicillin and 100 μg/mL streptomycin at 37ºC in humidified air with 5% CO_2. To test the biological activity of each BMP-2 polyhedra construct, polyhedra were spotted and desiccated on the bottom of wells of a culture plate (Iwaki). The seeding density of the cells was 3 x 10^3 cells/well in a 96-well culture plate, 2 x 10^4 cells/well in a 24-well culture plate and 1 x 10^6 cells/well in a 6-well culture plate. For assay of release of BMP-2, polyhedra were spotted and desiccated on a 0.4 μm pore size membrane cell culture insert (BD Biosciences). Cells were then seeded in each well of the cell culture plate.

Chondrogenic and osteogenic differentiation of ATDC5 cells

After cultivation, cells were washed with PBS, fixed with methanol for 20 min and incubated with alcian blue solution for 16 hours at room temperature. After washing with water, cell images were captured. In addition, stained cells were lysed with 6M guanidine hydrochloride solution and the absorbance of lysates was measured at 620 nm. For detection of mineralization, cells were cultured for 15 days or 28 days and fixed in methanol for 20 min. Cells were then stained with alizarin red solution for 16 hours at room temperature. Images were obtained by scanning the plate on a flat-bed scanner.

Assay of alkaline phosphatase (ALP) activity

Cultured cells in 96-well plates were rinsed with PBS, harvested by treatment with 0.05% trypsin-EDTA and then cells were solubilized with lysis buffer (10 mM NaOH, 0.2% Triton X-100). ALP activity was detected with LabAssay ALP (Wako Pure Chemical Industries) in

triplicate cultures according to the manufacturer's instructions. The dephosphorylation from p-nitrophenyl phosphate was monitored at 405 nm absorbance. A standard curve was prepared with p-nitrophenol. ALP units were defined as one nanomole of p-nitrophenol released per minute per DNA content. DNA concentration was determined with the QuantiFluor^{TM} dsDNA system (Promega).

Western Blot analysis

For detection of BMP-2 immobilized in polyhedra, purified polyhedra lysates were prepared by resuspending 4 x 10^4 polyhedra/μL in SDS-PAGE sample buffer (50 mM Tris/HCl, pH 8.0, 100 mM dithiothreitol, 2% SDS, 0.05% bromophenol blue and 10% glycerol), followed by boiling for 5 min.

For measurement of phosphorylated Smad1/5 in ATDC5 cells, confluent cultivated cells were stimulated with BMP-2 polyhedra or rhBMP-2 suspended in the culture medium and incubated for several time points at 37 ºC under 5% CO_2 in air. The stimulated cells were rinsed with ice-cold PBS and lysed in SDS-PAGE sample buffer. Lysates were then treated by sonic homogenization and boiled for 5min.

All samples were resolved by 12.5% SDS-PAGE and transferred to a nitrocellulose membrane at 1 mA/cm^2 for 90 min. For detection of BMP-2 or Smad1/5 proteins, the membranes were treated with primary antibody (anti-rhBMP-2 antibody, anti-phosphorylated Smad1/5 antibody and anti-Smad1/5 antibody) with a 1:1000 dilution. After washing three times, the membrane was incubated with a 1:3000 dilution of goat anti-mouse IgG conjugated to horseradish peroxidase (BioRad) for 2 hours at room temperature. Results were visualized by Chemilumi-One (Nacalai Tesque) and captured using an image scanner.

Preparation of atelocollagen sponges impregnated with BMP-2 polyhedra or rhBMP-2

We estimated that the average mass of BMP-2 immobilized in a polyhedron microcrystal (one cube) was ~ 2.8 x 10^{-5} ng (the average volume of a microcrystal is 5 x 5 x 5 μm^3). Hence, 3.6 x 10^7 microcrystals contained approximately 1 μg of recombinant protein. We mixed 1.8 x 10^7 or 3.6 x 10^6 BMP-2 polyhedra with 50 μL PBS and incorporated them into an atelocollagen sponge by air-drying for 12 hours at room temperature. The atelocollagen sponge, Pelnac® (Gunze), was cut into columns (diameter: 9 mm, height: 1 mm) and used for retention of polyhedra cubes and as a scaffold for bone regeneration. An atelocollagen sponge containing 1.8 x 10^7 or 3.6 x 10^6 CP-H polyhedra served as the control. A 50 μL aliquot of rhBMP-2 (Yamanouchi Pharmaceutical) solution prepared with 5 μg or 1 μg in PBS was dropped onto the sponge and left for 12 hours at 4 ^oC to make the rhBMP-2 atelocollagen sponge.

Surgical procedure

To study *in vivo* bone regeneration, we produced calvaria bone defects in 84 skeletally mature, 18-week-old, male Wistar rats weighing 350 - 400 g (Japan SLC). All rats were maintained at Kanagawa Dental College under strict pathogen-free conditions in accordance with the animal-study guidelines of the college. We sedated rats with an intraperitoneal injection of pentobarbital. A semilunar incision was then made in the scalp in the anterior region of the calvarium, allowing reflection of a full-thickness flap in the posterior direction. We prepared a 9 mm-diameter bone defect in the calvaria bone with a trephine bur (Technica) copiously irrigated with sterile saline water.

The 84 rats were divided into seven experimental groups consisting of 12 rats in each group. Group 1, 1.8 x 10^7 cubes of BMP-2 polyhedra; Group 2, 3.6 x 10^6 cubes of BMP-2 polyhedra; Group 3, 5 μg of rhBMP-2; Group 4, 1 μg of rhBMP-2; Group 5, 1.8 x 10^7 cubes of CP-H polyhedra; Group 6, 3.6 x 10^6 cubes of CP-H polyhedra; Group 7; No implant. The rats in each group were further divided into three groups (4 rats/group) depending on the

duration of the experiment (5, 10 and 15 weeks). Atelocollagen sponges were placed in the bone defects of each rat in experimental groups 1 to 6. After creating the defects and implanting the experimental atelocollagen sponges, the soft tissues were then repositioned and sutured with 4-0 nylon monofilament to achieve primary closure. In group 7, the bone defect was left to heal spontaneously without any implanted atelocollagen sponge (Fig. 12B-E).

Assessing bone regeneration

To assess bone regeneration, we euthanized rats with a lethal intravenous dose of pentobarbital after implantation. The area of the original surgical bone defect and surrounding tissues were removed *en bloc* and fixed in a 10% solution of neutral-buffered formalin. We produced images of all regions surrounding the calvaria bone defects by soft-X-ray radiography (Sofron Type SRO-M50, Soken) using electroscopic film (Fuji Photo Film). All images included a hydroxyapatite (HAp) step-wedge in order to correct for unequally developed film. We analyzed the soft-X-ray images with a program that analyses digital images (HC-2500/OL; WinROOF; Mitani) to determine the bone mineral content (BMC). The center of regenerated bone in the bone defect in each group was encircled by a closed line and the measurement area was specified. Blackening was measured in the area and the amount of HAp corresponding to this value was calculated.

μ-CT 3D reconstruction

Tissue specimens were scanned by μ-CT on a Scan Xmate-L090 (Comscan). Reconstructed images were analyzed with 3D-BON software (Ratoc System Engineering). Circular regions of 9 mm in diameter were cropped as the region of interest (ROI). Bone volume (BV) was then evaluated in the ROI.

Histological procedures and analysis

Tissue specimens were fixed in 10% formalin, decalcified in 22.5% formic acid solution, dehydrated with ethanol, and embedded in paraffin. We histologically observed 6 μm thin-sections stained with hematoxylin and eosin (HE) using an optical microscope (Olympus).

Statistical analysis

P values were computed with a Student's *t*-test. A *p*-value less than 0.05 was considered statistically significant.

Results

Construction of BMP-2 polyhedra

Most secreted molecules including growth factors, chemokines and cytokines do not diffuse far but are bound to the cell surface or surrounding extracellular matrices (ECM) to regulate cell function *in vivo* (Kanematsu et al., 2004; Macri et al., 2007; Schonherr and Hausser, 2000; Taipale and Keski-Oja, 1997). The ECM functions as a reservoir for various kinds of soluble growth factors. Indeed, ECM-bound growth factors are released from the ECM after proteolytic cleavage to alter cell behavior. Conversely, cells regulate degradation or remodeling of the ECM by secreting proteases and their inhibitors. Thus, the behavior of individual cells and tissue dynamics are regulated by intricate reciprocal interactions between cells and their surrounding micro-environment. Considering a dynamic complexity of the *in vivo* situation, there is an urgent need to develop new tools to reconstitute or modulate the extracellular micro-environment *in vitro*. In regenerative medicine, BMPs are delivered to the site of the fracture by incorporating them into a bone implant and they are released gradually to allow bone formation. Growth stimulation by BMPs must be localized and sustained for some weeks. Continuous and constant supplementation of BMP-2 is also necessary for bone

regeneration at the site of critical-sized bone defects. In this context, we hypothesized that BmCPV polyhedra could be utilized as a slow releasing agent of BMP-2.

BMP-2 exists as several forms: BMP-2 is expressed as a precursor of 396 amino acids (full-length BMP-2), the pro-form of BMP-2 (pro BMP-2) has no signal peptide, while mature BMP-2 is processed from the pro-form of BMP-2 (Fig. 11A). In this study, full-length, pro-form and mature BMP-2 were fused with VP3 or H1 tags and immobilized in BmCPV polyhedra (Fig. 11B). Mature BMP-2 was fused with VP3-S at the C-terminus, or VP3-L and H1 at the N-terminus. Pro BMP-2 was fused with VP3-S, -L, and H1 at the N-terminus. Full-length BMP-2 was fused with VP3-S at the C-terminus, or VP3-S, -L, and H1 at the N-terminus. As BMP-2 is known to act as a disulfide-linked homodimer and induces bone regeneration, BMP-2 polyhedra were produced using recombinant baculovirus expressing BmCPV polyhedrin and PDI. The immobilization of each form of BMP-2 into polyhedra was confirmed by performing SDS-PAGE and western blot analysis (data not shown).

Chondrogenic and osteogenic differentiation of ATDC5 cells by BMP-2 polyhedra

To evaluate whether BMP-2 polyhedra acted as a biologically active substance to enhance bone regeneration, we analyzed the effects of BMP-2 polyhedra on chondrogenic differentiation and phosphorylation of Smad1/5 in the ATDC5 cell line. ATDC5 cells are a suitable cell line for investigation of chondrogenic and osteogenic differentiation because early phases in culture display cartilage differentiation and late phases undergo bone differentiation.

A 24-well plate was spotted with desiccated BMP-2 polyhedra or empty polyhedra and ATDC5 cells were seeded on and around the polyhedron spot. Early phase differentiation of cartilage nodule formation was examined for the amount of sulfated glycosaminoglycan by alcian blue staining. Polyhedra containing full-length BMP-2 with VP3-S and H1 tags at the N-terminus promoted chondrogenic differentiation compared with the other BMP-2

polyhedra and empty polyhedra. During late phase osteogenic differentiation of ATDC5 cells, ECM is mineralized and exhibits characteristics similar to bone formation, which can be measured by alizarin red staining. Alizarin red staining was detected by ATDC5 cells cultivated with polyhedra containing pro BMP-2 with VP3-S and H1 at the N-terminus and full-length BMP-2 with VP3-S and H1 at the N-terminus. The latter showed the most induction of osteogenic differentiation. ALP activity of ATDC5 cells induced by polyhedra containing full-length BMP-2 with the H1 tag was also higher than other BMP-2 polyhedra (data not shown). We concluded that polyhedra containing full-length BMP-2 with the H1 tag (H1/fBMP-2 polyhedra) had a similar biological activity to BMP-2.

BMPs are members of the TGF-β superfamily and members of the Smad family of signal transduction molecules are components of a critical intracellular pathway that transmit TGF-β signals from the cell surface into the nucleus. Smad1/5 transmits BMP-2 signaling and forms a complex with Smad4 to allow translocation to the nucleus for gene regulation of bone-specific differentiation. To investigate the activation of the TGF-β and BMP signaling pathways, the phosphorylation of Smad1/5 in ATDC5 cells was examined using a phospho-Smad1/5 monoclonal antibody. Phosphorylation of Smad1/5 protein was observed after 1 hr in ATDC5 cells incubated with H1/fBMP-2 polyhedra and was maintained for 24 hrs. In contrast, these phosphorylation events were not evident in ATDC5 cells incubated with empty CP-H polyhedra.

Estimation of activity of H1/fBMP-2 polyhedra and assay of release of BMP-2 from H1/fBMP-2 polyhedra

BMP-2 activity of H1/fBMP-2 polyhedra was quantified by the amount of alcian blue staining of sulfated glycosaminoglycan, which shows the early differentiation phase of cartilage formation by ATDC5 cells, compared to the soluble form of recombinant human BMP-2 (rhBMP-2). Absorbance at 620 nm was increased by BMP-2 in a dose-dependent

manner. The maximum absorbance attained was at a dose of 31 ng/mL and alcian blue staining was inhibited by larger doses of rhBMP-2. BMP-2 activity from 3.6 x 10^7 cubes of H1/fBMP-2 polyhedra was estimated to be equivalent to the activity of 1 μg rhBMP-2.

H1/fBMP-2 polyhedra were spotted on the membrane of cell culture inserts and ATDC5 cells were seeded in each well of the cell culture plate. The late phase osteogenic differentiation of ATDC5 cells was assayed by ALP activity. ALP activity was dependent on the number of H1/fBMP-2 polyhedra in the cell culture insert and increased with dose. Osteogenic differentiation was more highly enhanced by H1/fBMP-2 polyhedra in the cell culture insert rather than H1/fBMP-2 polyhedra in proximity to cells. This indicated that BMP-2 is more efficiently released from H1/fBMP-2 polyhedra.

Clinical observations

All animals tolerated the surgical procedures without clinical signs of adverse reactions and were healthy during the entire experimental period.

Osteoinductive effects of H1/fBMP-2

X-ray radiographs of the calvaria bone defects at 5, 10, and 15 weeks after implantation showed the state of bone regeneration. At 5 weeks, radiopaque regions are clearly visible at the bone-defect sites where atelocollagen sponges containing sequestered H1/fBMP-2 polyhedron groups had been implanted. In contrast, radiopaque regions were not visible in the other experimental groups. At 10 and 15 weeks after implantation, the size of the radiopaque regions clearly showed that the largest amount of bone had formed at the bone-defect sites that received implanted atelocollagen sponges containing sequestered H1/fBMP-2 polyhedra. Radiographic analysis revealed that little or no bone regeneration took place in the rhBMP-2, empty polyhedra, and control groups during the 15-week period of this study. The BMC of tissue also clearly showed that more bone formed at bone-defect

sites that received implants of atelocollagen sponges with sequestered H1/fBMP-2 polyhedra than had formed at bone-defect sites in the rats in the other groups (Fig. 13A, B).

To evaluate the extent of bone regeneration after implantation, the calvaria bone specimens were harvested for μ-CT scanning and 3-D images were reconstructed. There was almost no regenerated bone in the bone defects in the rhBMP-2, empty polyhedra, and control groups except in the immediate vicinity of the bone-defect margins. This demonstrates that sequestered rhBMP-2 in atelocollagen sponges induced only a small amount of new bone regeneration. In contrast, when H1/fBMP-2 polyhedra was sequestered in atelocollagen sponges, significant regeneration took place. At 15 weeks after implantation, μ-CT images indicated healing in two of the four defects that had received 3.6×10^6 cubes of H1/fBMP-2 polyhedra. The other two defects demonstrated some bone regeneration but had not healed completely. In contrast, all bone defects implanted with atelocollagen sponges containing 1.8×10^7 H1/fBMP-2 polyhedra were completely healed. To quantify newly generated bone, we evaluated BV at 15 weeks after implantation by μ-CT scanning. Compared with the control group, the rhBMP-2 group had increased BV, but there was no significant difference between these two groups. In contrast, H1/fBMP-2 polyhedra significantly improved BV compared to the other groups. The mean BV in bone defects from the 1.8×10^7 H1/fBMP-2 polyhedra group was significantly higher than that of the 3.6×10^6 H1/fBMP-2 polyhedra group (Fig. 14A,B).

Histological analysis showed that atelocollagen sponges and polyhedron cubes remained in the fibrous connective tissue in sections of tissue taken from implanted atelocollagen sponges that contained 1.8×10^7 H1/fBMP-2 polyhedra at 5 weeks after implantation. New bone was formed in the atelocollagen sponges, but discontinuously from the edge of the host bone defect. However, at 15 weeks after implantation, histological analysis of the specimens revealed that the defects in which atelocollagen sponges containing 1.8×10^7 H1/fBMP-2 polyhedra had been implanted were filled with trabecular bone and that there was no

evidence of any remnants of atelocollagen sponge or polyhedron cubes. Regenerated bone was integrated with the host bone at the defect margins and supported a robust bone marrow. A lamellar bone pattern was visible in the regenerated bone tissues (Fig. 14C-E). These findings suggest that newly generated bone establishes mature bone tissue. Additionally, there was no evidence of inflammatory or foreign-body reaction from the host tissues adjacent to the new bone. These results suggest that implants of atelocollagen sponges containing H1/fBMP-2 polyhedra induced new bone formation in a dose- and time-dependent manner.

Discussion

In this study, we have shown that human full-length BMP-2 encapsulated via a H1-tag into polyhedra enhanced chondrogenic and osteogenic differentiation of progenitor ATDC5 cells. We also demonstrated that phosphorylation of endogenous Smad1/5 protein of ATDC5 cells was induced by H1/fBMP-2 polyhedra, indicating that the TGF-β and BMP signaling pathways are activated. These results suggest that H1/fBMP-2 polyhedra possess long-acting biological activity that enhances bone regeneration.

Critical-sized calvarial bone defects were then created by resecting periosteal fragments. Periosteal cells contain subsets of progenitor cells that possess the potential to differentiate into osteoblasts. Physical and chemical stimulation activates these periosteal cells and they produce new bone (Shimizu et al., 2001). In the no-implant and empty polyhedron control groups, bone repair did not proceed from the periosteum on the outer and inner surfaces near the bone defect. Conversely, H1/fBMP-2 polyhedra induced near complete repair of critical-sized calvarial bone defects.

To be maximally efficacious in regenerating bone, rhBMP-2 must be combined with a biomaterial matrix. Biomaterials need to be adequately porous to allow infiltration by cells and blood vessels and should be biocompatible, have low immunogenicity, be biodegradable,

be able to adhere to adjacent bone, and should retain the protein long enough to achieve healing (Brekke and Toth, 1998; Burg et al., 2000; Friess et al., 1999; Kirker-Head, 2000). Collagen sponge matrix containing rhBMP-2 promises to greatly enhance bone regeneration therapy.

Bovine-type collagen sponges as a carrier for rhBMP-2 are currently approved for clinical use by the U.S. Food and Drug Administration (Kanayama et al., 2006; Villavicencio et al., 2005). These delivery systems have been shown to enhance bone regeneration and to accelerate fracture healing, but they do not adequately control the release rate, often resulting in a high initial release of growth factor (Helm et al., 1997; Yang et al., 2004). BMP-2 has a short half-life *in vivo* and it is rapidly degraded (Zhao et al., 2006). The disadvantages of therapies using BMP-2 include its rapid degradation and diffusion *in vivo*, the cost of the high doses required for efficacy, and concerns over a correlation between high doses of rhBMP-2 and cancer incidence (Benglis et al., 2008; Cahill et al., 2009; Paramore et al., 1999). Consequently, milligram doses are often necessary for protein-based therapies, which can make such therapy so expensive that it may be unacceptable for clinical application.

Under physiological conditions, normal polyhedra are inert and insoluble (Belloncik and Mori, 1998; Rohrmann, 1986). These properties allowed us to employ these complexes as versatile micron-sized carriers of growth factors. We have demonstrated in this study that fBMP-2 polyhedra efficiently stimulate differentiation of ATDC5 cells. Thus, polyhedra immobilizing BMP-2 with a H1 tag are micron-sized bioactive substances. Release of BMP-2 from polyhedron cubes occurs as a result of the decay of BMP-2 polyhedra by proteases secreted from surrounding cells. Although we have not determined the optimal therapeutic dose of H1/fBMP-2 polyhedra for this application, we estimated that 3.6×10^7 H1/fBMP-2 polyhedra contained the equivalent of 1 μg of BMP-2 protein. We found that 3.6×10^6 or 1.8×10^7 cubes of H1/fBMP-2 polyhedra enhanced bone regeneration compared to the rhBMP-2 group. Statistical analysis showed that 1.8×10^7 H1/fBMP-2 polyhedra had a stronger effect

on bone regeneration than 3.6 x 10^6 H1/fBMP-2 polyhedra. It is therefore clear that there is a dose-dependent effect of BMP-2 delivered using this polyhedron delivery system.

It is important to design and improve delivery systems for growth factors. For many growth factors, their biological actions during physiologic events follow distinct patterns and only certain defined amounts of protein are released at predetermined times into the tissues. A slow-release system may be required because BMP-2 clearance might be faster than the bone-induction response of the host. In this study, histological examination showed polyhedron cubes were present in bone sections 10 weeks after implantation, but not at 15 weeks after implantation (data not shown). These results suggest that polyhedron particles were absorbed and BMP-2 protein was secreted for 10 or more weeks. Further, we suggest that the effects of bone regeneration can be prolonged by immobilization of BMP-2 in polyhedron particles and we demonstrate a means by which such particles might be applied in clinical therapy.

The basic requirement for a delivery system is that it does not produce any unexpected inflammatory reactions due to cytotoxicity or immunogenicity when used in human therapy. Histological examination showed that there was no evidence of inflammatory cells from the host tissues adjacent to the polyhedron cubes. Collagen sponge has a long safety history as a hemostatic agent and wound-covering material (Chvapil, 1977; Friess et al., 1996). Polyhedra are resistant to desiccation and they can easily be immobilized onto the surface of atelocollagen sponge (Matsushima et al., 2010). Our data suggest that applying polyhedra using atelocollagen sponges may improve bone regeneration therapy. For these reasons, insect polyhedron particles might provide a reliable growth factor delivery system, although further tests in large animals will be essential before it can proceed to the clinical setting.

Conclusions

Full-length, pro-form and mature BMP-2 was fused with VP3 or H1 tags and immobilized into BmCPV polyhedra. Chondrogenic and osteogenic differentiation of progenitor chondrogenic ATDC5 cells was enhanced by H1/fBMP-2 polyhedra, in which full-length BMP-2 was encapsulated by the H1 tag. Phosphorylation of Smad1/5 in ATDC5 cells was induced by H1/fBMP-2 polyhedra. It was estimated that 3.6 x 10^7 H1/fBMP-2 polyhedra contained an equivalent of 1 μg of BMP-2 protein. We created critical-sized calvarial bone defects by resecting periosteal fragments. Although little bone regeneration was observed at these critical-sized bone defects by atelocollagen sponges containing rhBMP-2 alone, H1/fBMP-2 polyhedra induced bone formation, almost entirely replacing the atelocollagen sponges and connecting the original bone with the regenerated bone. We conclude that use of polyhedra as a growth factor delivery system could advance the technology for bone regeneration.

References

Belloncik, S., and Mori, H. (1998). Cypovirus. In The insect viruses, L.K. Miller, and L.A. Ball, eds. (New York, Plenum Press), pp. 337-369.

Benglis, D., Wang, M.Y., and Levi, A.D. (2008). A comprehensive review of the safety profile of bone morphogenetic protein in spine surgery. Neurosurgery *62*, ONS423-431; discussion ONS431.

Bishop, G.B., and Einhorn, T.A. (2007). Current and future clinical applications of bone morphogenetic proteins in orthopaedic trauma surgery. Int Orthop *31*, 721-727.

Boerckel, J.D., Kolambkar, Y.M., Dupont, K.M., Uhrig, B.A., Phelps, E.A., Stevens, H.Y., Garcia, A.J., and Guldberg, R.E. (2011). Effects of protein dose and delivery system on BMP-mediated bone regeneration. Biomaterials *32*, 5241-5251.

Brekke, J.H., and Toth, J.M. (1998). Principles of tissue engineering applied to programmable osteogenesis. J Biomed Mater Res *43*, 380-398.

Burg, K.J., Porter, S., and Kellam, J.F. (2000). Biomaterial developments for bone tissue engineering. Biomaterials *21*, 2347-2359.

Cahill, K.S., Chi, J.H., Day, A., and Claus, E.B. (2009). Prevalence, complications, and hospital charges associated with use of bone-morphogenetic proteins in spinal fusion procedures. JAMA *302*, 58-66.

Chvapil, M. (1977). Collagen sponge: theory and practice of medical applications. J Biomed Mater Res *11*, 721-741.

Fiedler, J., Roderer, G., Gunther, K.P., and Brenner, R.E. (2002). BMP-2, BMP-4, and PDGF-bb stimulate chemotactic migration of primary human mesenchymal progenitor cells. J Cell Biochem *87*, 305-312.

Friess, W., Lee, G., and Groves, M.J. (1996). Insoluble collagen matrices for prolonged delivery of proteins. Pharm Dev Technol *1*, 185-193.

Friess, W., Uludag, H., Foskett, S., Biron, R., and Sargeant, C. (1999). Characterization of absorbable collagen sponges as rhBMP-2 carriers. Int J Pharm *187*, 91-99.

Helm, G.A., Sheehan, J.M., Sheehan, J.P., Jane, J.A., Jr., diPierro, C.G., Simmons, N.E., Gillies, G.T., Kallmes, D.F., and Sweeney, T.M. (1997). Utilization of type I collagen gel, demineralized bone matrix, and bone morphogenetic protein-2 to enhance autologous bone lumbar spinal fusion. J Neurosurg *86*, 93-100.

Jeon, O., Song, S.J., Kang, S.W., Putnam, A.J., and Kim, B.S. (2007). Enhancement of ectopic bone formation by bone morphogenetic protein-2 released from a heparin-conjugated poly(L-lactic-co-glycolic acid) scaffold. Biomaterials *28*, 2763-2771.

Jeppsson, C., Bostrom, M., and Aspenberg, P. (1999). Intraosseous BMP implants in rabbits. Inhibitory effect on bone formation. Acta Orthop Scand *70*, 77-83.

Kanayama, M., Hashimoto, T., Shigenobu, K., Yamane, S., Bauer, T.W., and Togawa, D. (2006). A prospective randomized study of posterolateral lumbar fusion using osteogenic

protein-1 (OP-1) versus local autograft with ceramic bone substitute: emphasis of surgical exploration and histologic assessment. Spine (Phila Pa 1976) *31*, 1067-1074.

Kanematsu, A., Marui, A., Yamamoto, S., Ozeki, M., Hirano, Y., Yamamoto, M., Ogawa, O., Komeda, M., and Tabata, Y. (2004). Type I collagen can function as a reservoir of basic fibroblast growth factor. J Control Release *99*, 281-292.

Kirker-Head, C.A. (2000). Potential applications and delivery strategies for bone morphogenetic proteins. Adv Drug Deliv Rev *43*, 65-92.

Lutolf, M.P., Weber, F.E., Schmoekel, H.G., Schense, J.C., Kohler, T., Muller, R., and Hubbell, J.A. (2003). Repair of bone defects using synthetic mimetics of collagenous extracellular matrices. Nat Biotechnol *21*, 513-518.

Macri, L., Silverstein, D., and Clark, R.A. (2007). Growth factor binding to the pericellular matrix and its importance in tissue engineering. Adv Drug Deliv Rev *59*, 1366-1381.

Matsushima, K., Suyama, T., Takenaka, C., Nishishita, N., Ikeda, K., Ikada, Y., Sawa, Y., Jakt, L.M., Mori, H., and Kawamata, S. (2010). Secreted frizzled related protein 4 reduces fibrosis scar size and ameliorates cardiac function after ischemic injury. Tissue Eng Part A *16*, 3329-3341.

Meikle, M.C. (2007). On the transplantation, regeneration and induction of bone: the path to bone morphogenetic proteins and other skeletal growth factors. Surgeon *5*, 232-243.

Mont, M.A., Ragland, P.S., Biggins, B., Friedlaender, G., Patel, T., Cook, S., Etienne, G., Shimmin, A., Kildey, R., Rueger, D.C., *et al.* (2004). Use of bone morphogenetic proteins for musculoskeletal applications. An overview. J Bone Joint Surg Am *86-A Suppl 2*, 41-55.

Paramore, C.G., Lauryssen, C., Rauzzino, M.J., Wadlington, V.R., Palmer, C.A., Brix, A., Cartner, S.C., and Hadley, M.N. (1999). The safety of OP-1 for lumbar fusion with decompression-- a canine study. Neurosurgery *44*, 1151-1155; discussion 1155-1156.

Petite, H., Viateau, V., Bensaid, W., Meunier, A., de Pollak, C., Bourguignon, M., Oudina, K., Sedel, L., and Guillemin, G. (2000). Tissue-engineered bone regeneration. Nat Biotechnol *18*, 959-963.

Reddi, A.H. (1994). Symbiosis of biotechnology and biomaterials: applications in tissue engineering of bone and cartilage. J Cell Biochem *56*, 192-195.

Reddi, A.H. (1997). BMPs: actions in flesh and bone. Nat Med *3*, 837-839.

Rizzi, S.C., Ehrbar, M., Halstenberg, S., Raeber, G.P., Schmoekel, H.G., Hagenmuller, H., Muller, R., Weber, F.E., and Hubbell, J.A. (2006). Recombinant protein-co-PEG networks as cell-adhesive and proteolytically degradable hydrogel matrixes. Part II: biofunctional characteristics. Biomacromolecules *7*, 3019-3029.

Rohrmann, G.F. (1986). Polyhedrin structure. J Gen Virol *67 (Pt 8)*, 1499-1513.

Saito, N., Okada, T., Horiuchi, H., Murakami, N., Takahashi, J., Nawata, M., Ota, H., Nozaki, K., and Takaoka, K. (2001). A biodegradable polymer as a cytokine delivery system for inducing bone formation. Nat Biotechnol *19*, 332-335.

Schmitt, J.M., Hwang, K., Winn, S.R., and Hollinger, J.O. (1999). Bone morphogenetic proteins: an update on basic biology and clinical relevance. J Orthop Res *17*, 269-278.

Schonherr, E., and Hausser, H.J. (2000). Extracellular matrix and cytokines: a functional unit. Dev Immunol *7*, 89-101.

Shimizu, T., Sasano, Y., Nakajo, S., Kagayama, M., and Shimauchi, H. (2001). Osteoblastic differentiation of periosteum-derived cells is promoted by the physical contact with the bone matrix in vivo. Anat Rec *264*, 72-81.

Taipale, J., and Keski-Oja, J. (1997). Growth factors in the extracellular matrix. FASEB J *11*, 51-59.

Villavicencio, A.T., Burneikiene, S., Nelson, E.L., Bulsara, K.R., Favors, M., and Thramann, J. (2005). Safety of transforaminal lumbar interbody fusion and intervertebral recombinant human bone morphogenetic protein-2. J Neurosurg Spine *3*, 436-443.

Yang, X.B., Whitaker, M.J., Sebald, W., Clarke, N., Howdle, S.M., Shakesheff, K.M., and Oreffo, R.O. (2004). Human osteoprogenitor bone formation using encapsulated bone morphogenetic protein 2 in porous polymer scaffolds. Tissue Eng *10*, 1037-1045.

Zabka, A.G., Pluhar, G.E., Edwards, R.B., 3rd, Manley, P.A., Hayashi, K., Heiner, J.P., Kalscheur, V.L., Seeherman, H.J., and Markel (2001). Histomorphometric description of allograft bone remodeling and union in a canine segmental femoral defect model: a comparison of rhBMP-2, cancellous bone graft, and absorbable collagen sponge. J Orthop Res *19*, 318-327.

Zhao, B., Katagiri, T., Toyoda, H., Takada, T., Yanai, T., Fukuda, T., Chung, U.I., Koike, T., Takaoka, K., and Kamijo, R. (2006). Heparin potentiates the in vivo ectopic bone formation induced by bone morphogenetic protein-2. J Biol Chem *281*, 23246-23253.

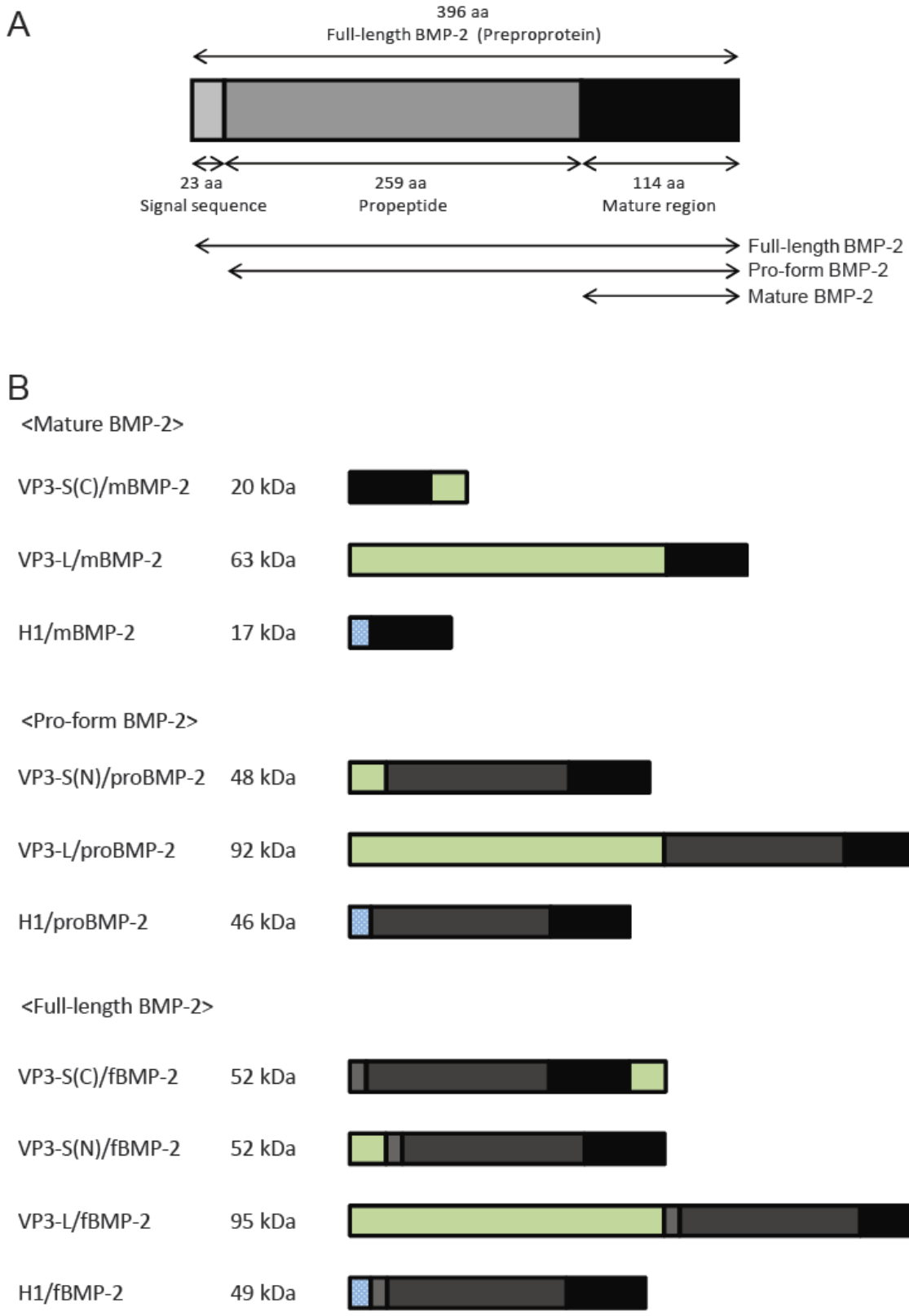

Fig. 11. Recombinant BMP-2 for encapsulation into BmCPV polyhedra. (A) Full-length BMP-2 (396 aa) consists of a signal sequence (25 aa), a propeptide (259 aa), and a mature region (114 aa). (B) Full-length, pro-form and mature BMP-2 were fused with VP3 or H1 tags and immobilized into BmCPV polyhedra.

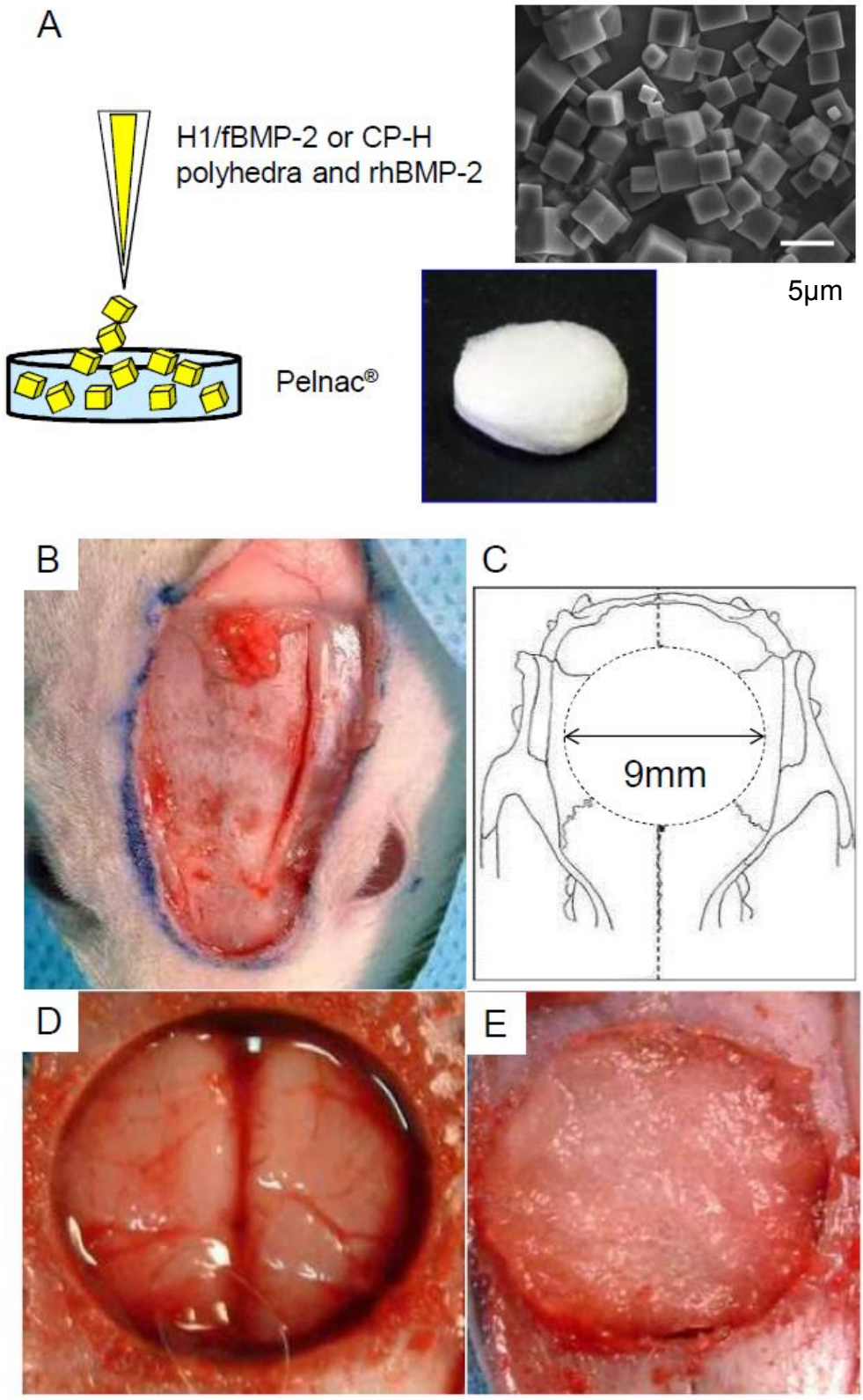

Fig. 12. Surgical procedure for *in vivo* bone regeneration. (A) H1/fBMP-2 polyhedra, CP-H polyhedra, or rhBMP-2 were dropped onto atelocollagen Pelnac® sponges. (B) The skin and underlying tissues including the periosteum were resected to expose the calvarial bone. (C, D) Critical-sized defects (9 mm in diameter) were created on the calvarial bone. (E) An atelocollagen sponge was implanted into the bone defect.

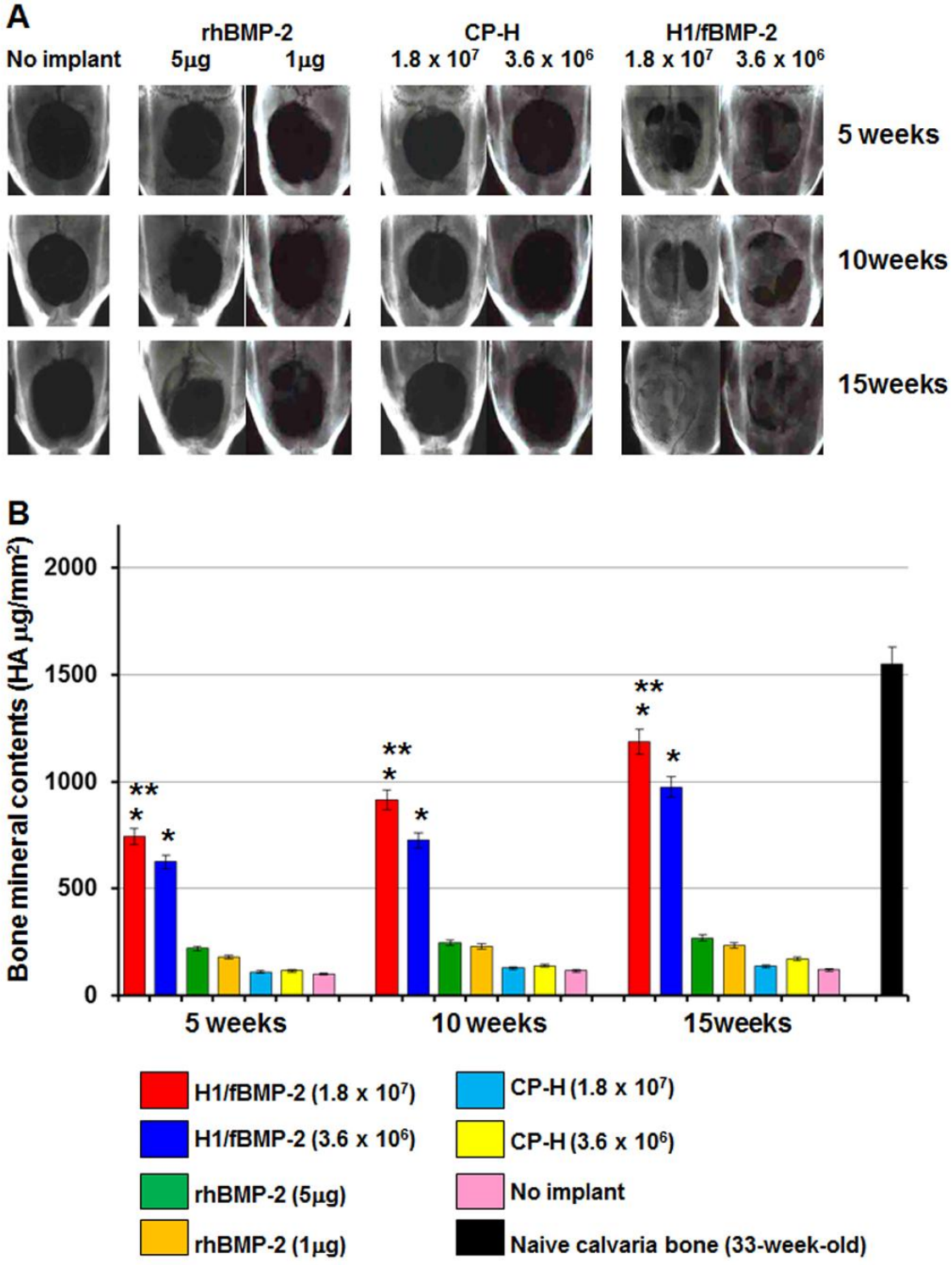

Fig. 13. Radiographic appearance of the calvarial bone defects after application of no implant (No implant), atelocollagen sponge with rhBMP-2 (rhBMP-2), atelocollagen sponge with empty polyhedra (CP-H), and atelocollagen sponge with H1/fBMP-2 polyhedra (H1/fBMP-2). (A) Sequential radiographic photos showed bone regeneration at 5, 10, and 15 weeks after implantation in the H1/fBMP-2 experimental group. (B) The bone mineral content (BMC) of the calvarial bone defects after implantation. BMC is shown at 5, 10, and 15 weeks after implantation.

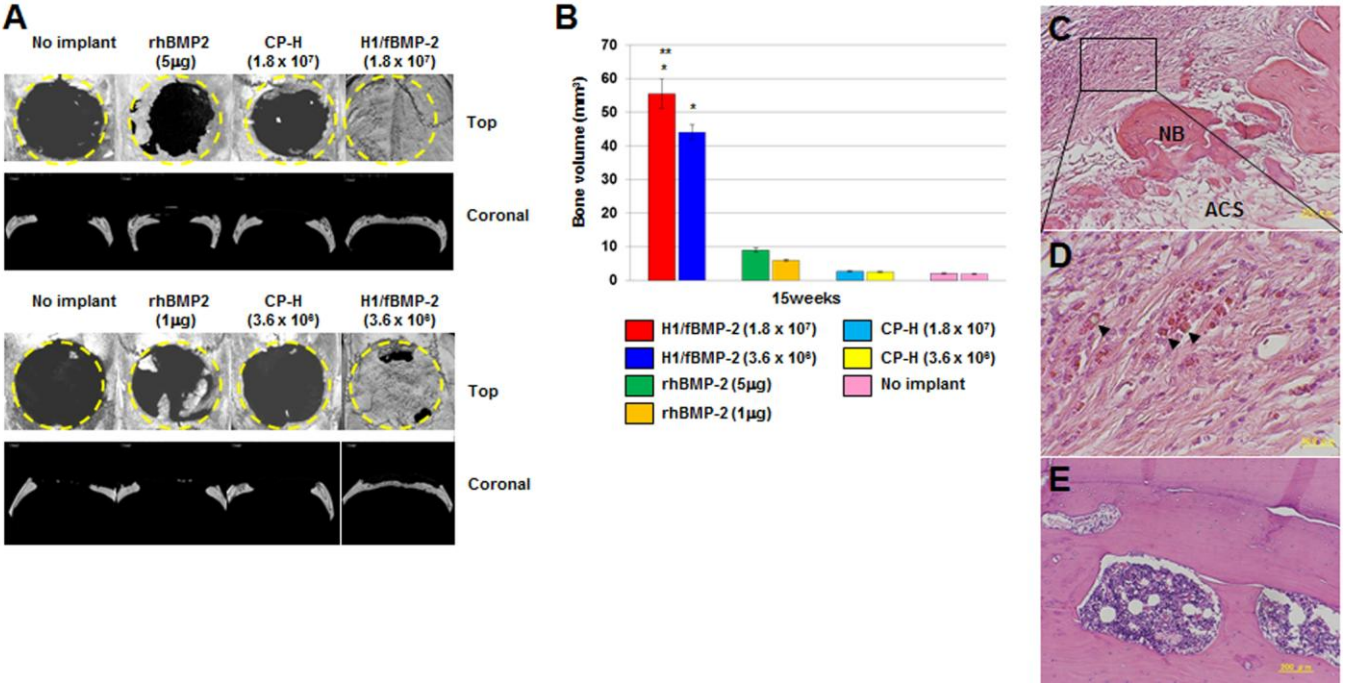

Fig. 14. Bone formation in critical-sized calvarial defects 15 weeks after implantation. (A) μ-CT analysis was performed to visualize and quantify bone regeneration. 3-D images were reconstructed to illustrate the top and coronal section views of no implant (No implant), atelocollagen sponge with rhBMP-2 (rhBMP-2), atelocollagen sponge with empty polyhedra (CP-H), and atelocollagen sponge with H1/fBMP-2 polyhedra (H1/fBMP-2). The dotted line represents the surgical margins of the calvaria bone defect. (B) Newly generated bone was evaluated by bone volume (BV) in bone defects assessed from the projected area of the μ-CT images. Histological sections of the bone defects obtained 5 weeks after implantation of the atelocollagen sponge with 1.8 x 10^7 H1/fBMP-2 polyhedra. (C, D) New bone (NB) formation was induced in atelocollagen sponges (AC). Many polyhedra remained in the fibrous connective tissue. Arrows indicate polyhedra. Insert shows a high magnification image. Photomicrograph of the bone defects at 15 weeks following implantation of the atelocollagen sponge with H1/fBMP-2 polyhedra. (E) Newly generated bone was entirely replaced by trabecular bone with hematopoietic bone marrow 15 weeks after implantation.

Chapter 4: 3D co-cultures of keratinocytes and melanocytes and cytoprotective effects on keratinocytes to ROS by insect virus-derived protein microcrystals

The epidermis is composed of four layers, stratum basale, stratum spinosum, stratum granulosum, and stratum corneum (Costin and Hearing, 2007). Stratum basale, which consists of basal keratinocytes, Merkel cells and melanocytes, is a single layer attached to a noncellular basement membrane that separates the epidermis from the dermis. The epidermis is made up of cells formed by differentiation from migrating keratinocytes of the stratum basale (Costin and Hearing, 2007). A variety of cytokines and growth factors is bound to the basement membrane, which is made up mainly of collagen IV, laminin, proteoglycans and glycosaminoglycans, and released to the construction of the epidermis (Brohem et al., 2011). We hypothesized that it was necessary to mimic the release of cytokines from the basement membrane and control the direction of cytokine traffic in three dimensional (3D) co-cultures of keratinocytes and melanocytes.

In this study, we evaluated FGF-2 polyhedra and FGF-7 polyhedra for activity in 3D cell cultures of keratinocytes and melanocytes. Furthermore, the cytoprotective effects of FGF-7 polyhedra on keratinocytes exposed to reactive oxygen species (ROS) were investigated.

Materials and methods

FGF-7 or FGF-2 polyhedra

FGF-7 or FGF-2 encapsulated polyhedra can be made by use of H1-tag or VP3-tag to immobilize foreign proteins into cypovirus polyhedral (Ijiri et al., 2009). In this study we used polyhedra in which FGFs were encapsulated via H1-tag. For comparison of FGF-7 polyhedra with recombinant human FGF-7 (rhFGF-7) or the growth supplement, each number of FGF-7 polyhedra was mounted on the surface of each well of a 96-well plate.

Keratinocytes (1,000 cells/well) were cultured on FGF-7 polyhedra in 0.1 mL of the basal medium. The same numbers of keratinocytes were also cultured in 0.1 mL of the basal medium containing each dose of rhFGF-7 or the growth supplement.

Co-cultures of keratinocytes and melanocytes

To establish 3D co-cultures, after 2.5 x 10^4 numbers of FGF-2 polyhedra and 2.5 x 10^6 numbers of FGF-7 polyhedra were mixed in 250 μL of Cellmatrix Type I-A (Nitta Gelatin), the collagen gels were poured into IWAKI cloning rings (RING-12) in a 6-well plate and incubated for 1 hr at 37 ^oC in 5 % CO_2. Collagen gels containing 2.5 x 10^6 numbers of cytokine-free polyhedra (empty polyhedra) were also prepared. Defined Keratinocyte-SFM (Invitrogen) was used as a basal medium and the basal medium containing 1.2 mM Ca^{2+} was used as a differentiation medium. To each well, 4 mL of the basal medium was added and then 2 x 10^5 normal human epidermal keratinocytes (KURABO) and 2 x 10^4 normal human epidermal melanocytes (KURABO) suspended in 200 μL of the basal medium were put on the collagen gels. After 24 hrs at 37 ^oC, the basal medium was replaced with 4 mL of the differentiation medium. After 16 hrs at 37 ^oC, cloning rings were removed and the differentiation medium was discarded. For air-exposed culture, 1 mL of the differentiation medium was added followed by incubation for 2 weeks with the differentiation medium replaced every 2 days. As a control, 3D co-cultures of keratinocytes and melanocytes on the collagen gels containing empty polyhedra were incubated with the basal and differentiation medium containing 1 ng/mL of rhFGF-2 and 100 ng/mL of rhFGF-7. Frozen sections of 3D cultured keratinocytes and melanocytes were subjected to propidium iodide staining, hematoxylin and eosin staining, and Fontana-Masson staining.

Cytoprotective effects of FGF-7 polyhedra for keratinocytes

After 4 x 10^6 numbers of FGF-7 polyhedra were mounted on the surface of each well of a 6-well plate, keratinocytes (2 x 10^5 cells) were cultured on FGF-7 polyhedra to confluence in 2 mL of the basal medium. Defined Keratinocyte-SFM Growth Supplement (Invitrogen) was used as a growth supplement instead of FGF-7 polyhedra or rhFGF-7. Keratinocytes were also cultured to confluence in 2 mL of the basal medium containing 4 μL of the growth supplement. ROS in keratinocytes treated with menadione at 6.25, 12.5 and 25 μM was detected by ROS Detection Reagent (Invitrogen) and analyzed by microscopy and flow cytometry Guava PCA-96 (Millipore). Phosphorylated and unphosphorylated Akt were detected by use of Phospho-Akt (ser473) (D9E) rabbit mAb (Cell Signaling Technology) and Akt (pan) (C67E7) rabbit mAb (Cell Signaling Technology), respectively. Superoxide dismutase (SOD) activities were assayed by SOD Assay Kit-WST (DOJINDO). Aeroxiredoxin 6 (Prdx6) was detected by use of Prdx6 mouse mAb (Abcam).

Results and discussion

3D cell cultures of keratinocytes and melanocytes

We tested whether FGF-2 polyhedra and FGF-7 polyhedra were available to the co-culture of keratinocytes and melanocytes. Melanin biosynthesis is a complex pathway that appears in melanocytes which contain membrane-bound organelles referred to as melanosomes. Melanosomes are transferred *via* dendrites to surrounding keratinocytes, where they play a critical role in photoprotection (Costin and Hearing, 2007). When keratinocytes and melanocytes were co-cultured with FGF-2 polyhedra and FGF-7 polyhedra, the dendrites-like structures were observed from some melanocytes (Fig. 15a), suggesting that FGF-2 and FGF-7 encapsulated polyhedra induce the interaction of melanocytes with keratinocytes.

Keratinocytes and melanocytes were cultured on type 1 collagen gels containing FGF-2 polyhedra and FGF-7 polyhedra with the basal medium. After replacement with the basal

medium containing Ca^{2+} (differentiation medium), air-exposed incubation was continued for 2 weeks. Both cells were also cultured onto the collagen gels containing empty polyhedra with the basal and differentiation medium containing rhFGF-2 and rhFGF-7. Epidermal differentiation was induced at the air-liquid interface and enucleation of keratinocytes was confirmed by propidium iodide stain (Fig. 16). Fontana-Masson stain revealed that melanin was formed in the upper layer of the 3D cultures with rhFGF-2 and rhFGF-7 (Fig. 16). The 3D cultures with rhFGFs as skin models were clearly different from the epidermis. However, in the 3D cultures with FGF-2 polyhedra and FGF-7 polyhedra, melanin was observed at the bottom layer of the 3D cultures. These results suggest that 3D cultures of keratinocytes and melanocytes with FGF-2 polyhedra and FGF-7 polyhedra are useful as an *in vitro* human skin model.

Cytoprotective effects of FGF-7 polyhedra for keratinocytes exposed to ROS

The inositol triphosphate (PI3) kinase/Akt pathway is known to be an important survival pathway in many cell types, such as neurons, fibroblasts, and keratinocytes (Blume-Jensen et al., 1998; Decraene et al., 2002; Dudek et al., 1997; Mildner et al., 2002; Romashkova and Makarov, 1999; Wan et al., 2001; Yao and Cooper, 1995). Activation of PI3 kinase results in increased levels of phosphatidylinositol-3,4,5-triphosphate and inositol 3,4-biphosphate, which ultimately leads to the activation of the serine-threonine kinase Akt/PKB (Kandel and Hay, 1999). Activated Akt inhibits apoptosis, particularly the intrinsic apoptotic pathway. Cytoprotection of keratinocytes by FGF-7 has been reported and its anti-apoptotic effect is considered to be linked to activation of the PI3 kinase/Akt pathway (Braun et al., 2004). We have previously reported that FGF-7 polyhedra, as well as rhFGF-7, have a potent cytoprotective effect on keratinocytes exposed to UV radiation. Cytoprotective effects by FGF-7 polyhedra for keratinocytes treated with menadione, which is a generator of ROS, were investigated. Keratinocytes were cultured with the basal medium containing FGF-7

polyhedra or the growth supplement. The growth supplement was conventionally used instead of rhFGF-7 for culture of keratinocytes. Proliferation of keratinocytes by FGF-7 polyhedra or the growth supplement was similar (Fig. 15b), but ROS generation by menadione was different for FGF-7 polyhedra compared to the growth supplement (Fig. 17a). FGF-7 polyhedra strongly inhibited ROS generation by menadione and the cytoprotective effect was considered to be dependent on the activation of the PI3 kinase/Akt pathway (Fig. 17b).

Expression of SOD is known to be up-regulated through the PI3 kinase/Akt pathway (Rojo et al., 2004; Zhang et al., 2012). SOD activities of keratinocytes treated with menadione were measured. The SOD activities of keratinocytes proliferated with FGF-7 polyhedra were higher than those of the growth supplement (Fig. 17c). FGF-7 also regulates the enhancement of the antioxidative capacity by an increase of the antioxidant enzyme peroxiredoxin 6 (Prdx6) in dermal epithelium (Kumin et al., 2006). Prdx6 has an important role in antioxidant defense as a scavenger of H_2O_2 and other hydroperoxides (Fisher, 2010). Expression of Prdx6 was stimulated by the treatment of menadione, but the up-regulation of Prdx6 expression in addition of FGF-7 polyhedra was higher than that of the growth supplement (Fig. 17C). Up-regulation of SOD activity tentatively causes an increase of H_2O_2 in keratinocytes treated with FGF-7 polyhedra, but overexpression of Prdx6 rapidly degrades H_2O_2 and protects from ROS-induced cytotoxity. We conclude that the PI3 kinase/Akt pathway and Prdx6 as a scavenger of hydroperoxides are strongly activated in keratinocytes cultured with FGF-7 polyhedra for antioxidant defense.

Polyhedra are highly resistant to both nonionic and ionic detergents and are insoluble at neutral pH (Coulibaly et al., 2007). Cytokines immobilized into polyhedra are stable against desiccation and can be kept at room temperature for several years. Because excessive accumulation of ROS can lead to cell aging and severe cell damage, the cells in the skin are

equipped with a network of antioxidant enzymes to counteract oxidative stress and to maintain their redox balance. Here we would like to propose the use of FGF7 polyhedra for counteraction to oxidative stress and activation of a network of antioxidant enzymes.

Conclusions

When keratinocytes and melanocytes were co-cultured on the gel containing FGF-2 polyhedra and FGF-7 polyhedra followed by air-lifting, the melanin was observed at the bottom layer of the 3D cultures of keratinocytes and melanocytes. FGF-7 polyhedra induced the overexpression of superoxide dismutase and peroxiredoxin 6 and provided a potent cytoprotective effect to keratinocytes.

Referenses

Blume-Jensen, P., Janknecht, R., and Hunter, T. (1998). The kit receptor promotes cell survival via activation of PI 3-kinase and subsequent Akt-mediated phosphorylation of Bad on Ser136. Curr Biol *8*, 779-782.

Braun, S., auf dem Keller, U., Steiling, H., and Werner, S. (2004). Fibroblast growth factors in epithelial repair and cytoprotection. Philos Trans R Soc Lond B Biol Sci *359*, 753-757.

Brohem, C.A., Cardeal, L.B., Tiago, M., Soengas, M.S., Barros, S.B., and Maria-Engler, S.S. (2011). Artificial skin in perspective: concepts and applications. Pigment Cell Melanoma Res *24*, 35-50.

Costin, G.E., and Hearing, V.J. (2007). Human skin pigmentation: melanocytes modulate skin color in response to stress. FASEB J *21*, 976-994.

Coulibaly, F., Chiu, E., Ikeda, K., Gutmann, S., Haebel, P.W., Schulze-Briese, C., Mori, H., and Metcalf, P. (2007). The molecular organization of cypovirus polyhedra. Nature *446*, 97-101.

Decraene, D., Agostinis, P., Bouillon, R., Degreef, H., and Garmyn, M. (2002). Insulin-like growth factor-1-mediated AKT activation postpones the onset of ultraviolet B-induced apoptosis, providing more time for cyclobutane thymine dimer removal in primary human keratinocytes. J Biol Chem *277*, 32587-32595.

Dudek, H., Datta, S.R., Franke, T.F., Birnbaum, M.J., Yao, R., Cooper, G.M., Segal, R.A., Kaplan, D.R., and Greenberg, M.E. (1997). Regulation of neuronal survival by the serine-threonine protein kinase Akt. Science *275*, 661-665.

Fisher, A.B. (2010). Peroxiredoxin 6: a bifunctional enzyme with glutathione peroxidase and phospholipase A(2) activities. Antioxid Redox Signal *15*, 831-844.

Ijiri, H., Coulibaly, F., Nishimura, G., Nakai, D., Chiu, E., Takenaka, C., Ikeda, K., Nakazawa, H., Hamada, N., Kotani, E., *et al.* (2009). Structure-based targeting of bioactive proteins into

cypovirus polyhedra and application to immobilized cytokines for mammalian cell culture. Biomaterials *30*, 4297-4308.

Kandel, E.S., and Hay, N. (1999). The regulation and activities of the multifunctional serine/threonine kinase Akt/PKB. Exp Cell Res *253*, 210-229.

Kumin, A., Huber, C., Rulicke, T., Wolf, E., and Werner, S. (2006). Peroxiredoxin 6 is a potent cytoprotective enzyme in the epidermis. Am J Pathol *169*, 1194-1205.

Mildner, M., Eckhart, L., Lengauer, B., and Tschachler, E. (2002). Hepatocyte growth factor/scatter factor inhibits UVB-induced apoptosis of human keratinocytes but not of keratinocyte-derived cell lines via the phosphatidylinositol 3-kinase/AKT pathway. J Biol Chem *277*, 14146-14152.

Rojo, A.I., Salinas, M., Martin, D., Perona, R., and Cuadrado, A. (2004). Regulation of Cu/Zn-superoxide dismutase expression via the phosphatidylinositol 3 kinase/Akt pathway and nuclear factor-kappaB. J Neurosci *24*, 7324-7334.

Romashkova, J.A., and Makarov, S.S. (1999). NF-kappaB is a target of AKT in anti-apoptotic PDGF signalling. Nature *401*, 86-90.

Wan, Y.S., Wang, Z.Q., Shao, Y., Voorhees, J.J., and Fisher, G.J. (2001). Ultraviolet irradiation activates PI 3-kinase/AKT survival pathway via EGF receptors in human skin in vivo. Int J Oncol *18*, 461-466.

Yao, R., and Cooper, G.M. (1995). Requirement for phosphatidylinositol-3 kinase in the prevention of apoptosis by nerve growth factor. Science *267*, 2003-2006.

Zhang, R., Chae, S., Lee, J.H., and Hyun, J.W. (2012). The cytoprotective effect of butin against oxidative stress is mediated by the up-regulation of manganese superoxide dismutase expression through a PI3K/Akt/Nrf2-dependent pathway. J Cell Biochem *113*, 1987-1997.

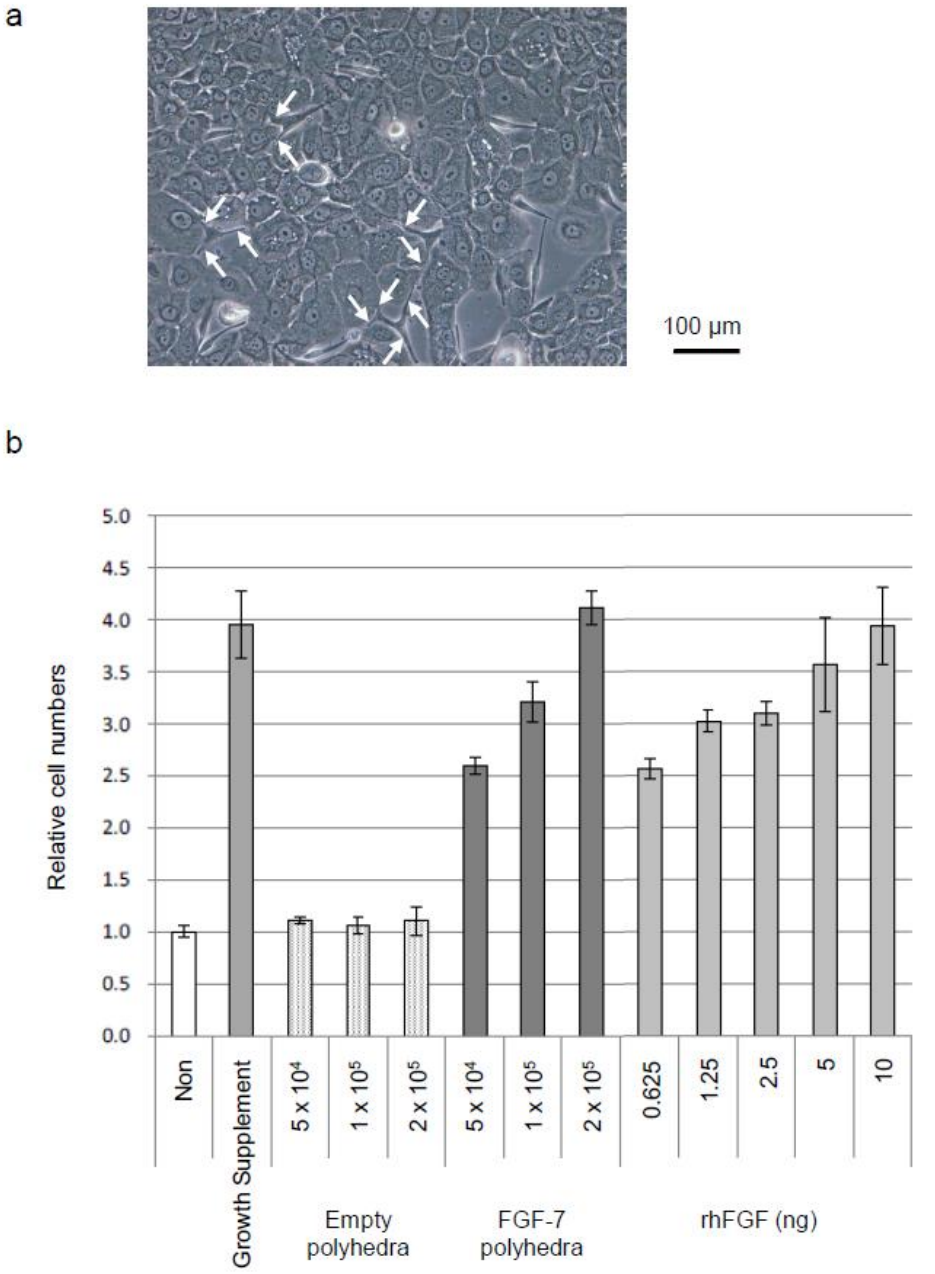

Fig. 15. Culture of keratinocytes and melanocytes by use of FGF-2 polyhedra and FGF-7 polyhedra. (a) Each number of FGF-2 polyhedra (4 x 10^4 numbers) and FGF-7 polyhedra (4 x 10^6 numbers) were mounted on the surface of each well of a 6-well plate. Keratinocytes (2 x 10^5 cells) and melanocytes (2 x 10^4 cells) were plated into each well of the 6-well plate. The co-culture was incubated for 5 days in 2 mL of the basal medium replaced every 2 days. Arrows show the dendrites-like structures from melanocytes. (b) For comparison of FGF-7 polyhedra with rhFGF-7 or the growth supplement, each number of FGF-7 polyhedra was mounted on the surface of each well of a 96-well plate. Keratinocytes (1,000 cells/well) were cultured on FGF-7 polyhedra in 0.1 mL of the basal medium. The same numbers of keratinocytes were also cultured in 0.1 mL of the basal medium containing each dose of rhFGF-7 or the growth supplement.

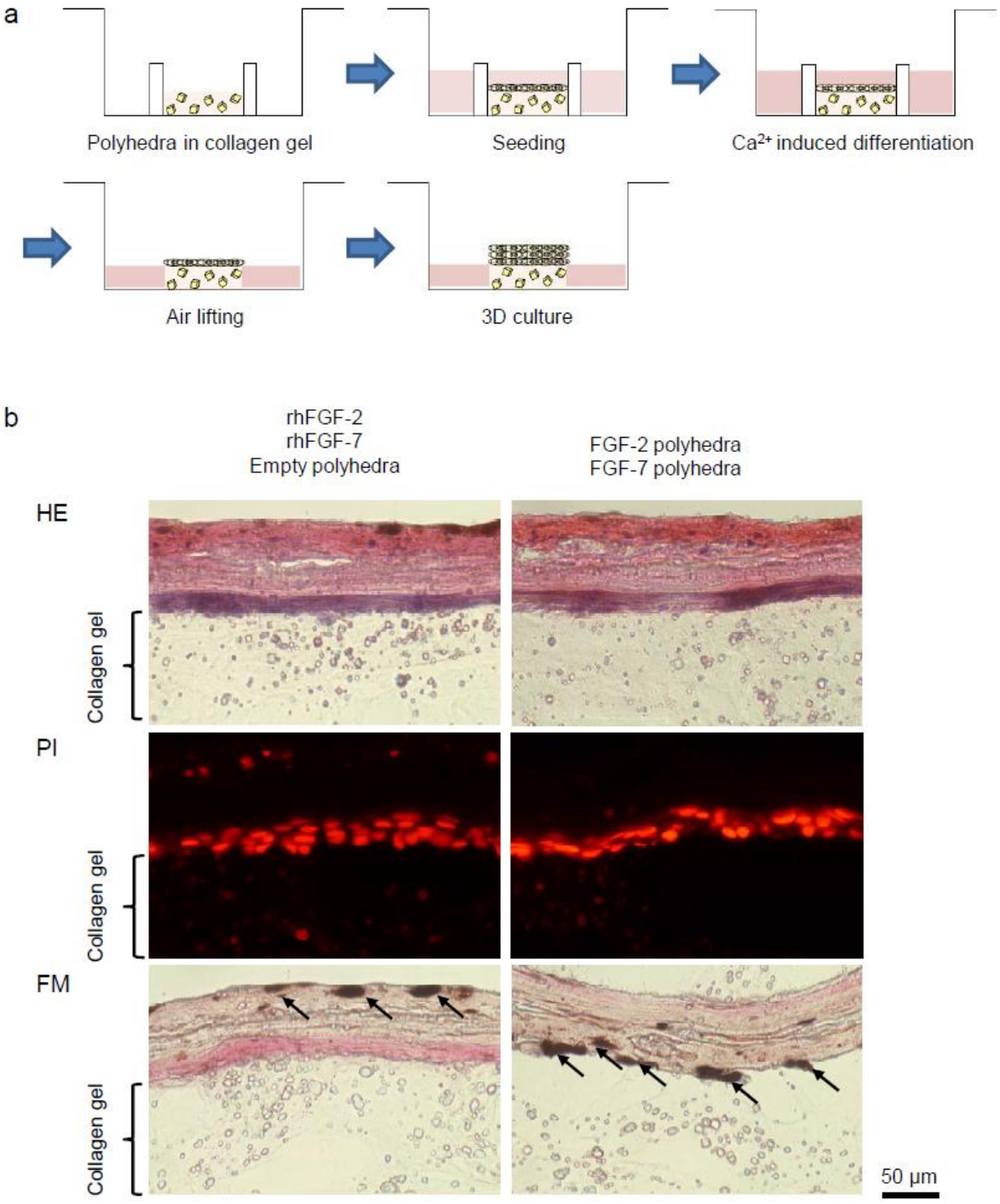

Fig. 16. 3D co-culture of keratinocytes and melanocytes. Keratinocytes and melanocytes were cultured and differentiated on a collagen gel containing empty polyhedra in the basal and differentiation medium supplied with rhFGF-2 and rhFGF-7 (left panels). The same 3D co-cultures were performed on a collagen gel containing FGF-2 polyhedra and FGF-7 polyhedra in the growth and differentiation medium without FGFs (right panels) PI, propidium iodide stain (for nuclei); HE, hematoxylin and eosin stain; FM, Fontana-Masson stain (for melanin). Arrows show the formation of melanin.

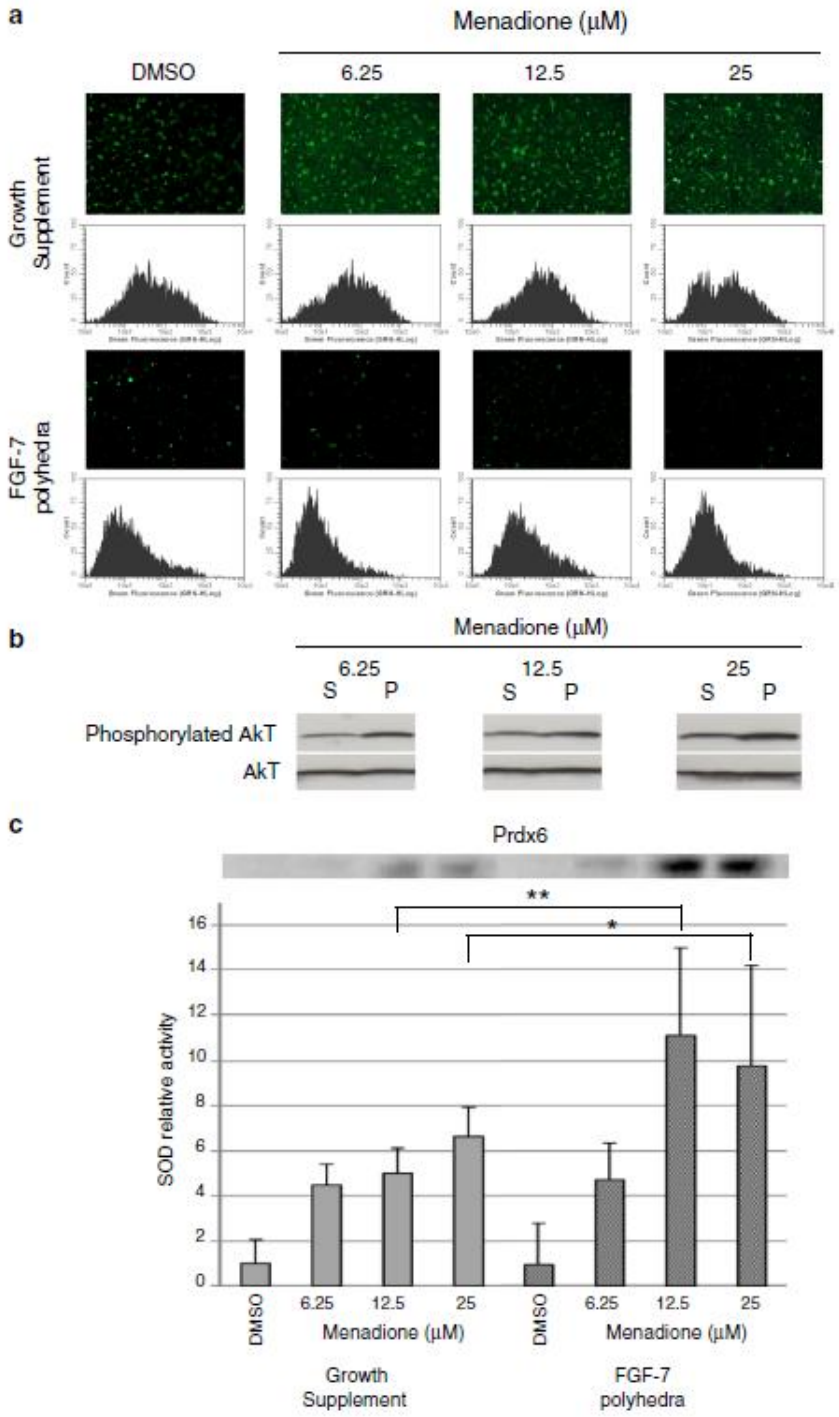

Fig. 17. Cytoprotection of keratinocytes from menadione by FGF-7 polyhedra. Keratinocytes were cultured in the basal medium containing FGF-7 polyhedra or the growth supplement (Sup). Menadione was added at final concentrations of 6.25, 12.5 and 25 μM. (a) After ROS Detection Reagent was added to menadione-treated keratinocytes, ROS was detected by microscopy (upper) and analyzed by flow cytometry (lower). (b) Phosphorylated and unphosphorylated Akt in menadione-treated cells were detected by phospho-Akt rabbit mAb and Akt rabbit mAb, respectively. (c) Peroxiredoxin 6 was detected by Prdx6 mouse mAb. SOD activities in menadione-treated cells were measured by SOD Assay Kit-WST.